โครงการ

การเรียนการสอนเพื่อเสริมประสบการณ์

ชื่อโครงการ รามานสเปคโตรสโคปีของกราฟีนวาเนเดียมไดออกไซด์เฮทเทอโรสตรัคเจอร์

Raman Spectroscopy of Graphene/VO_2 Heterostructure

ชื่อนิสิต น.ส. วิรัญชนา รัตนสกุลดิลก **เลขประจำตัว** 5933445323

ภาควิชา ฟิสิกส์

ปีการศึกษา 2562

คณะวิทยาศาสตร์ จุฬาลงกรณ์มหาวิทยาลัย

Raman Spectroscopy of Graphene/VO_2 Heterostructure

A Senior Project Presented to

Department of Physics

The Faculty of Science

Chulalongkorn University

In Partial Fulfillment

of the Requirements for the Degree of

Bachelor of Science

---

by

Wirunchana Rattanasakuldilok

May, 2020

Project Title: Raman Spectroscopy of Graphene/VO_2 Heterostructure

Name: Wirunchana Rattanasakuldilok **ID:** 5933445323

Advisor: Salinporn Kittiwatanakul, Ph.D.

Department: Physics

Academic Year: 2019

This report is in partial fulfillment of the requirements for the degree of Bachelor of Science, Department of Physics, Faculty of Science, Chulalongkorn University, academic year 2019.

Approved by committees

..... Chair of Committee

(Assoc. Prof. Sukkaneste Tungasmita, Ph.D.)

..... Committee

(Chayanit Asawatangtrakuldee, Ph.D.)

..... Advisor

(Salinporn Kittiwatanakul, Ph.D.)

Acknowledgements

First and foremost, I would like to express my gratitude to Prof. Salinporn Kittiwatanakul, my advisor, for guiding me in the research process and teaching me how to improve myself as a physics student. I would like to express my appreciation to Mr. Kittipat Hiraprayoonpong for helping me carry out the graphene exfoliation. It is very kind of you to cheer me up and even try to bring new angles to my experiment. Additionally, I am very grateful to Mr. Thanut Kaewsuksri for helping me with the mini-hotplates and cracking many problems together. I would also like to give special thanks to Mr. Teerachote Pakornchote for his time and invaluable advice on Raman spectroscopy. Finally, I could never have gone through all of this without support from my family and friends. Thank you mom and dad for teletubbying me and indulging me with great food and coffee. Thank you bro and sis for bearing with me. Thank you DeeDee for always being there and shining rainbows to my banal days. Thank you Minnie for your midnight Line call, compassion, and hilarious stories. Thank you Nanki for sharing me funny vibes and being such a great partner. Thank you.

Contents

1. Introduction 1
1.1. Motivation 1
1.2. Objectives 1
2. Background 2
2.1 Vanadium dioxide 2
2.2 The metal-insulator transitions of VO_2 2
2.2.1 The electronic band structures of R-VO_2 3
2.2.2 Peierls phase transition 5
2.2.3 Mott phase transition 7
2.2.4 Peierls-Mott phase transition 8
2.3 Graphene 8
2.4 Hybridization of VO_2 and graphene 12
2.5 Raman spectroscopy 15
2.5.1 Raman shifts of VO_2 18
2.5.2 Raman shifts of graphene 22
3. Experiments 26
3.1 VO_2 fabrication 26
3.2 Resistance vs temperature 27
3.3 Graphite exfoliation 27
3.4 Raman spectroscopy 28
3.5 Temperature-dependent Raman spectroscopy 29
4. Results and discussion 30
4.1. VO_2/Al_2O_3 samples 30
4.2. Resistance vs temperature 31
4.3. Raman spectra of VO_2/Al_2O_3 32
4.4. Graphite exfoliation 32
4.5. Raman spectra of bilayer-graphene/VO_2/Al_2O_3 33
4.6. Temperature-dependent Raman spectra of bilayer-graphene/SiO_2, VO_2/Al_2O_3, and bilayer-graphene/VO_2/Al_2O_3 35
5. Summary 39
References 40

บทคัดย่อ

วาเนเดียมไดออกไซด์เป็นโลหะแทรนซิชันออกไซด์ที่มีการเปลี่ยนแปลงโครงสร้างและคุณสมบัติการนำไฟฟ้าที่อุณหภูมิสูงกว่าอุณหภูมิห้องเล็กน้อยประมาณ 340 K เพื่อปรับปรุงประสิทธิภาพของวาเนเดียมไดออกไซด์ จึงมีการสร้างเฮทเทอโรสตรัคเจอร์ของวาเนเดียมไดออกไซด์และกราฟีน อย่างไรก็ตามฟิลม์ที่ได้มักจะมีคุณภาพต่ำ ซึ่งเป็นผลจากกระบวนการปลูกวาเนเดียมไดออกไซด์บนกราฟีน ในงานวิจัยนี้จึงได้มีการเปลี่ยนลำดับชั้นของฟิลม์โดยให้กราฟีนซึ่งได้มาจากกระบวนการการลอกชั้นของกราไฟต์วางอยู่บนวาเนเดียมไดออกไซด์ที่ปลูกบนแซฟไฟร์ โดยวาเนเดียมไดออกไซด์ที่ใช้จะมีความหนาต่างกัน คือ 50 nm และ 100 nm โครงสร้างผสมที่ได้จะถูกนำไปวิเคราะห์ด้วยรามานสเปคโตรสโคปีเพื่อศึกษาผลกระทบที่กราฟีนและวาเนเดียมไดออกไซด์มีต่อกัน และสำหรับโครงสร้างผสมที่ใช้วาเนเดียมไดออกไซด์ที่มีความหนามากกว่า จะถูกนำไปศึกษาด้วยรามานสเปคโตรสโคปีที่มีการเปลี่ยนแปลงอุณหภูมิเพื่อสังเกตการเปลี่ยนแปลงของอุณหภูมิแทรนซิชัน และถูกนำไปเปรียบเทียบกับผลรามานที่มีการเปลี่ยนแปลงอุณหภูมิของวาเนเดียมไดออกไซด์ที่ไม่มีกราฟีนและของกราฟีนบนซิลิกอนไดออกไซด์ จากผลการทดลอง กราฟีนที่ได้จากกระบวนการการลอกชั้นของกราไฟต์เป็นกราฟีนแบบสองชั้น โดยผลรามานบ่งชี้ว่ากราฟีนทำให้เกิดความเค้นแรงดึงในแนวระนาบในวาเนเดียมไดออกไซด์ ขณะเดียวกันวาเนเดียมไดออกไซด์ที่มีความบางกว่าจะทำให้เกิดความเครียดอัดในกราฟีนแบบสองชั้นมากกว่าเนื่องจากแลตทิซพารามิเตอร์ของแซฟไฟร์ที่เล็กกว่าแลตทิซพารามิเตอร์ของกราฟีน จากการศึกษาด้วยรามานสเปคโตรสโคปีที่มีการเปลี่ยนแปลงอุณหภูมิ พบว่าการเปลี่ยนแปลงโครงสร้างเกิดขึ้นก่อนการเปลี่ยนแปลงคุณสมบัติการนำไฟฟ้าและพบว่าการเปลี่ยนแปลงนี้ไม่มีเฟส M2 อย่างไรก็ตาม ผลของกราฟีนที่มีต่ออุณหภูมิแทรนซิชันของวาเนเดียมไดออกไซด์นั้นไม่สามารถสรุปได้จากข้อมูลรามาน โดยสันนิษฐานว่าการที่อุณหภูมิแทรนซิชันของวาเนเดียมไดออกไซด์ที่มีกราฟีนไม่มีการเปลี่ยนแปลงอย่างชัดเจนนั้นเป็นผลจากการเพิ่มของจำนวนอิเล็กตรอนในวาเนเดียมไดออกไซด์ที่มาจากกราฟีน นอกจากนี้ จีแบนด์ (G-band) ของกราฟีนเลื่อนไปทางน้ำเงินเมื่ออุณหภูมิเพิ่มขึ้นในบางช่วง ซึ่งแตกต่างกับการเลื่อนไปทางแดงจากผลของกราฟีนสองชั้นบนซิลิกอนไดออกไซด์

คำสำคัญ วาเนเดียมไดออกไซด์, กราฟีน, รามานสเปคโตรสโคปี

Abstract

Vanadium dioxide (VO_2) is a very interesting transition metal oxide as it undergoes structural-phase and insulator-to-metal transitions just above room temperature (~340 K). Synthesizing VO_2 on top of graphene to enhance the performance of VO_2 has long been practiced; however, the quality of the obtained films is usually degraded. In this research, the layer order was switched, with bilayer graphene fabricated via graphite exfoliation lying on top of VO_2/Al_2O_3 of 2 different VO_2 thicknesses, 50 nm and 100 nm. The obtained hybrids were studied via Raman spectroscopy to see how the materials affect one another. The hybrid of the thicker sample was further investigated using temperature-dependent Raman spectroscopy to observe the change in transition temperature and compared with the graphene-absent sample and bilayer graphene on silicon dioxide. From graphite exfoliation, there are only bilayer-graphene flakes available on both 50-nm and 100-nm VO_2. The Raman results clearly indicate that bilayer graphene induces the in-plane tensile stress in VO_2, and the VO_2 thickness influences the compressive strain in bilayer graphene due to a smaller lattice parameter of the sapphire substrate compared with that of graphene. From the temperature-dependent Raman experiment, the structural transition apparently takes place before the electrical transition. Although the effect of bilayer graphene on the transition temperature cannot be deduced from this experiment, for which the countereffect of electron injection from graphene might account, some interesting features are observed: the transition is direct with no M2 intermediate state, and the G-band of bilayer graphene blue shifts for some increasing temperatures, as opposed to a usual red shift seen in bilayer graphene on SiO_2.

Keywords: vanadium dioxide, graphene, Raman spectroscopy

1. Introduction

1.1 Motivation

VO_2 has acquired a lot of attentions due to its reversible metal-insulator transition (MIT) at ~340 K accompanied by a structural phase transition (SPT) and change in optical and electrical properties. Several attempts have been made to optimize its properties for possible applications. One interesting method is to couple it with graphene, a 2-D material known for its high strength, bendability, and excellent electrical conductivity. However, a usual hybrid structure is VO_2 on top of graphene, of which inevitable drawbacks could dull the practical uses. Additionally, there is no research in the inverse structure of graphene/VO_2 previously reported, leaving many questions as to how the new structure might be and what properties might be affected.

In this project, the layer order would be switched to avoid the defects from a normal VO_2/graphene synthesis and to study the properties of both materials after the hybridization. VO_2 deposited on Al_2O_3 substrate was previously prepared via reactive bias target ion beam deposition (RBTIBD) at University of Virginia, and exfoliated graphene would be transferred onto VO_2/Al_2O_3 using an adhesive tape. Al_2O_3 is favoured as the substrate due to its hexagonal crystal lattice which is similar to that of graphene. The microstructure of different-VO_2-thickness (50 and 100 nm) hybrid films would be studied via Raman spectroscopy in order to determine the effect of graphene on VO_2 and vice versa. Besides, (100 nm)VO_2/Al_2O_3, graphene/(100 nm)VO_2/Al_2O_3, and graphene/SiO_2 would be further analyzed via temperature-dependent Raman spectroscopy to investigate the effect of graphene on VO_2 transition temperature (T_{MIT}) and the effects of the substrates on graphene as the temperature changes. The T_{MIT} of (100 nm)VO_2/Al_2O_3 obtained from Raman spectroscopy would also be compared with that from resistance-variation-with-temperature method in case of different electrical and structural transitions. Provided that VO_2 has good crystallinity, the possible change of T_{MIT} from temperature-dependent Raman together with Raman shifts after hybridization would also help clarify the contribution of graphene-induced strain to the VO_2 transition.

1.2 Objectives

a. To synthesize thin film of graphene deposited on VO_2/Al_2O_3 by exfoliation method
b. To analyze the microstructures of graphene/VO_2/Al_2O_3 with different VO_2 thickness (50 and 100 nm) via Raman spectroscopy and compare them to graphene-absent VO_2/Al_2O_3
c. To analyze the phase-transition properties of graphene/(100 nm)VO_2/Al_2O_3 via temperature-dependent Raman spectroscopy and compare them to graphene-absent (100 nm)VO_2/Al_2O_3
d. To analyze the effect of VO_2 on graphene structure compared with graphene on SiO_2

2. Background

2.1 Vanadium dioxide

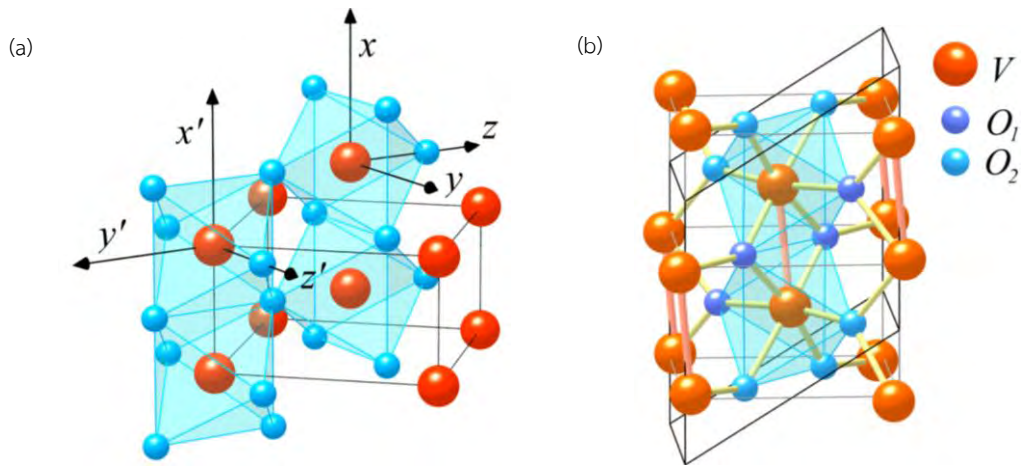

Fig 1. The crystal structure of VO_2. (a) R phase (Red and blue atoms correspond to vanadium and oxygen atoms respectively.) (b) M1 phase.[1]

For decades, vanadium dioxide (VO_2) is well known for its reversible metal-insulator transition (MIT) at ~340 K along with its structural phase transition (SPT). Consequently, there are abrupt changes in electrical conductivity and optical transmittance in the infrared region of VO_2. These near-room-temperature transition properties make VO_2 a perfect material for various technologies such as thermochromic coating, memory devices, phase-change switches, sensors and field-effect transistors.[1]

Above the MIT temperature (T_{MIT}), VO_2 conducts electricity and reflects IR. It possesses a rutile structure (R phase) as indicated in Fig 1(a). It has a body-centered tetragonal unit cell with lattice constants $a_r = b_r = 0.455$ nm and $c_r = 0.286$ nm.[2] Each of the vanadium atoms is surrounded by six oxygen atoms forming an octahedral compound. As the temperature falls below T_{MIT}, the crystal structure becomes monoclinic (M1 phase) accompanied by a significant drop in the carrier density and an upsurge in IR transparency. As shown in Fig 1(b)., the vanadium atoms dimerize along the original c_r-axis tilting with respect to the c_r-axis, while the oxygen atoms stay roughly at the same positions. To include both vanadium atoms of the dimer, the new unit cell is twice as large as the original rutile primitive unit cell. The insulating phase's lattice parameters are $a_{M1} = 0.575$ nm, $b_{M1} = 0.452$ nm, $c_{M1} = 0.538$ nm, and $\beta = 122.6°$.[2]

It is also worth pointing out that the T_{MIT} and T_{SPT} are very sensitive to a substrate type, crystallinity of VO_2, doping, and the interfacial strain between VO_2 and the substrate.[2,3]

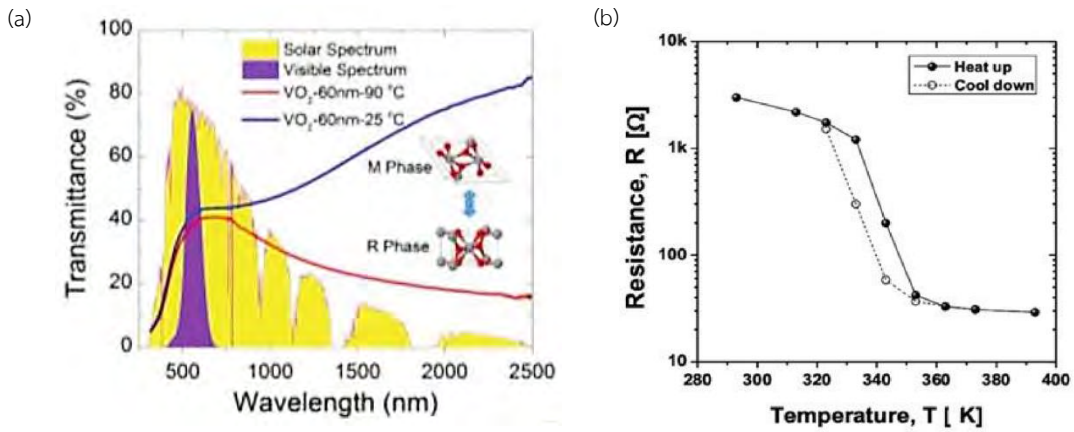

Fig 2. (a) The UV-VIS-IR percent transmittance of VO_2. The yellow background indicates solar irradiance at sea level.[4] (b) Resistance as a function of temperature of VO_2.[5]

2.2 The metal-insulator transitions of VO_2

2.2.1 The electronic band structures of R-VO_2

In the R phase, there are 2 vanadium cations V^{4+} and 2 oxygen anions O^{2-} per unit cell.[6] The electron configurations of vanadium and oxygen are [Ar] $3d^3$ $4s^2$ and [He] $2s^2$ $2p^4$ respectively.[7] Each vanadium atom forms 6 sigma bonds with its oxygen octahedron, leaving $3d^1$ electron behind. For the whole crystal, these 3d orbitals become a 3d band. Since oxygen has a full $2p^6$ orbital and each VO_2 molecule contributes only 1 valence electron, the 3d band is partially filled and hence allows electrical conduction in the R phase.

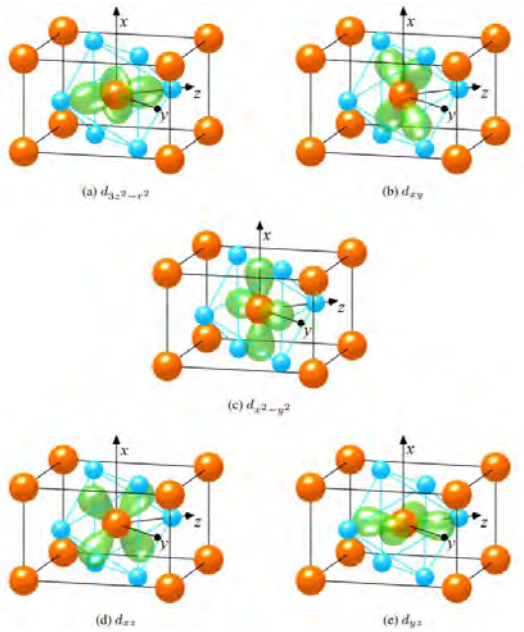

Fig 3. The orientations of degenerate d orbitals in the R phase. The red atoms are vanadium and the blue atoms are oxygen.[1]

Taking a closer look into the d orbitals, they are 5-fold degenerate unless vanadium and oxygen atoms reside together in a crystal. (Spin degeneracy is excluded.) As depicted in Fig 3., each d orbital experiences a different array of point charges of oxygen ligands in space. The first 2 orbitals, namely $d_{3z^2-r^2}$ (Fig 3(a).) and d_{xy} (Fig 3(b).), have maximum charge density in the direction of ligand vertices. According to crystal field theory, the electrostatic repulsion between these ligands and the $d_{3z^2-r^2}$ and d_{xy} orbitals is stronger than that with other d orbitals. Consequently, an energy level of the original degenerate orbitals is split into two with the higher level called the e_g level ($d_{3z^2-r^2}$ and d_{xy} orbitals) and the lower level called the t_{2g} level ($d_{x^2-y^2}$, d_{xz}, and d_{xy} orbitals). The t_{2g} band is now the conduction band of the crystal.[8]

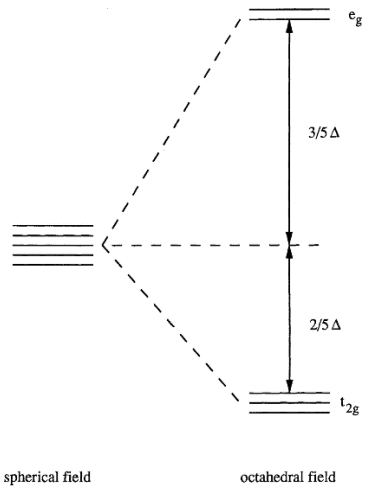

Fig 4. A diagram explains crystal field splitting in an octahedral structure.[8]

Furthermore, due to an electron interaction between nearest neighbor vanadium atoms, the t_{2g} band is further split. As the lobe of $d_{x^2-y^2}$ points toward other $d_{x^2-y^2}$ orbitals of neighboring vanadium atoms in c_r direction, a strong sigma bond can be formed. On the other hand, possible orbital overlaps of d_{yz} are a weaker sigma bond with its consecutive d_{yz} orbitals in <100> direction and a pi bond with the oxygen ligands, while only pi bonding with the ligands is allowed for d_{xz}. This results in lifted degeneracy of 2 overlapping energy bands comprising of the higher π^* band from the initial d_{yz} and d_{xz}, and the lower $d_{||}$ band from the original $d_{x^2-y^2}$.[1,2,4,7,8] The Fermi level of this band structure is shown in Fig 5.(right).[11]

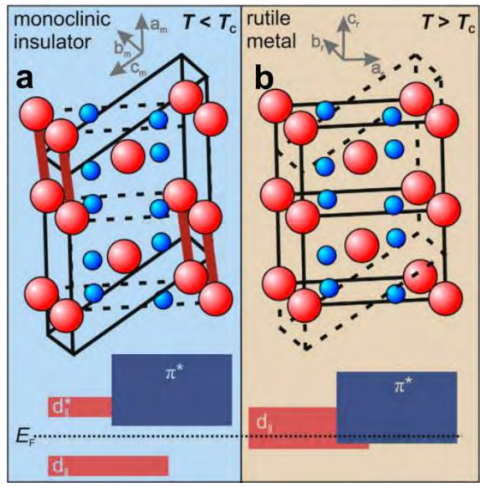

Fig 5. The crystal structure of VO_2 and its energy band. The red atoms are vanadium and the blue atoms are oxygen. (left) M1 phase (right) R phase[11]

2.2.2 Peierls phase transition

Across the MIT, Goodenough assumed that the structural distortion is sufficient to open up a band gap. Two components of this structural change are considered to account for the insulating energy band in Fig 5.(left): V-V pairing and antiferroelectric distortion.[1] The metal-metal pairing within the vanadium chains along the c_r axis causes splitting of the $d_{||}$ band into filled bonding and empty antibonding states. Additionally, the displacement perpendicular to the c_r axis and parallel to the rutile <110> directions enhances p-d orbital overlap, which in turn levels up the π^* band.

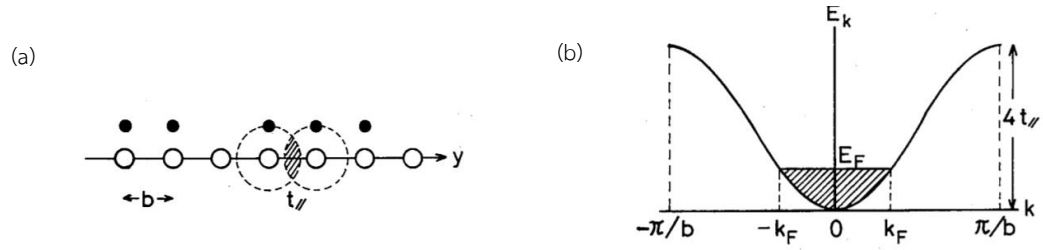

Fig 6. 1-D electron system (a) Classical electron picture. The open and closed circles display atoms and electrons respectively. (b) Band diagram.[12]

To understand the effect of the V-V pairing on the split of the $d_{||}$ band, Peierls transition of 1-D crystal must be examined. The simplest situation is displayed in Fig 6.(a), where a chain of equally spaced atoms with n electrons per site is explained by a tight-binding model. In this tight-binding approximation, the atoms are considered weakly interacting and electrons are tightly bound to their atoms, implying that the atomic orbitals remain almost intact.[13] With a nearest-neighbor approximation, each electron is pictured as if it hops from its site to other nearest sites. The Hamiltonian of this system is

$$H = -t \sum_{<i,j>,\sigma} (c_{i,\sigma}^{\dagger} c_{j,\sigma} + h.c.) \quad (1)$$

where t (or $t_{\parallel}$ in Fig 4.) is a hopping or overlap integral, <i,j> is a nearest neighbor index, $\boldsymbol{\sigma}$ is spin polarization, $\boldsymbol{c}^{\dagger}$is an electron creation operator, and $\boldsymbol{c}$ is an electron annihilation operator. It can be seen from Fig 6.(a) and in equation (1) that the overlap integral $t_{\parallel}$ determines the strength of the hopping. If $t_{\parallel}$ is large enough, electrons are no longer localized, and hence the electrical conduction. After diagonalizing this hopping Hamiltonian, the cosine energy band diagram in the first Brillouin zone with a bandwidth of $4t_{\parallel}$ can be obtained as depicted in Fig 6.(b). As Fermi wave vector k_F equals to $n\pi/2b$, the band is partially filled for n<2, meaning this 1-D crystal is metal.[12]

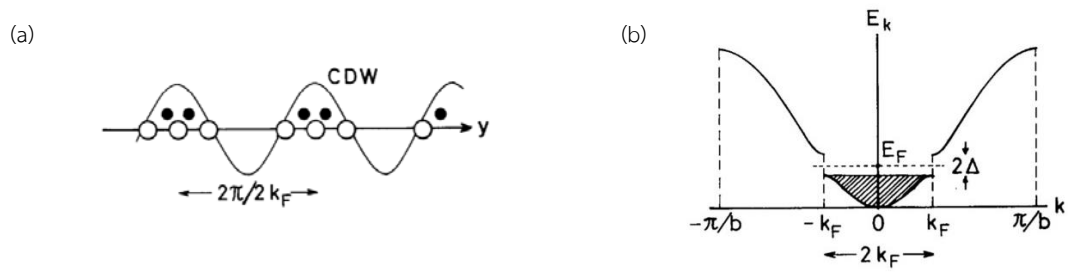

Fig 7. 1-D electron system (a) Classical electron picture. The open and closed circles display atoms and electrons respectively. (b) Band diagram.[12]

However, this 1-D system is unstable at low temperatures due to the interaction between the electrons and the lattices. This phenomenon, prominent when thermal excitation is reduced, stems from the greater energy dissipation for the bandgap opening compared with that for ion rearrangement.[2] As shown in Fig 7.(a), lattice distortion occurs with the new lattice constant $2\pi/2k_F$. Since the current unit cell is twice as large as the former one and contains 2 electrons, the size of the first Brillouin zone is now $2k_F$,and a bandgap opens at the Fermi level (Fig 7.(b)). This 1-D crystal becomes an insulator.[12]

In summary, the V-V dimerization is believed to open the $d_{\parallel}$ bandgap based on the Peierls phase transition. This theory is supported by a correct band calculation using LDA theory[14] (Fig 8.), although a contradiction of optical-gap values arises. While LDA predicts the gap of -0.04 eV, the actual gap has a much higher value of 0.6 eV. Besides, there are other questions regarding the appearance of a metastable phase (M2 phase) and the magnetic features of the MIT which are still unanswered by the Peierls transition.[2] This leads to another proposed mechanism, Mott phase transition.

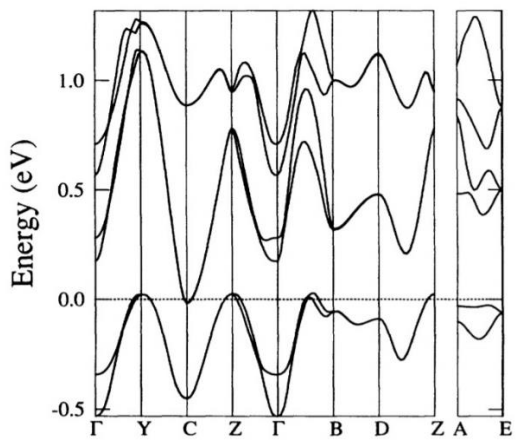

Fig 8. The band diagram of the M1 phase computed by LDA.[14]

2.2.3 Mott Phase Transition

In the Peierls transition, the key mechanism is centered at the electron-lattice interaction. On the contrary, Mott transition is based on electron-electron correlations. For these correlations, a modified version of the Hamiltonian in equation (1) called Hubbard Hamiltonian is considered. The Hubbard Hamiltonian can be written as

$$H = -t \sum_{<i,j>,\sigma} (c_{i,\sigma}^{\dagger} c_{j,\sigma} + h.c.) + U \sum_{i} n_{i,\uparrow} n_{i,\downarrow} \quad (2)$$

where $n_{i,\sigma} = c_{i,\sigma}^{\dagger} c_{i,\sigma}$ and U is Hubbard energy. The additional term on the right represents Coulomb repulsion between electrons on the same site. If short-range Coulomb interactions overcome the hopping energy (U >> t), electrons are localized and the system is insulator. With this condition, the system is insulator even the energy band is half filled. In the case of VO_2, Zylbersztejn and Mott suggested that these correlations are efficiently screened by the π^* band in the metallic phase. Once the π^* band is lifted higher as a result of V-V zigzagged distortion, the electron-electron correlations come into play and the $d_{\parallel}$ band is split. According to this model, a modified calculation called LDA+U yields a satisfying bandgap: the calculated band diagram is consistent with that achieved from experiments, and the magnetic nature of M2 phase is correctly predicted.

All in all, this model proposes the additional Hubbard energy term for the existence of the wide bandgap and the intermediate phases. Nevertheless, the conductivity of the R phase and a non-magnetic property of both R and M1 phases are still unexplained by this mechanism.[2]

2.2.4 Peierls-Mott Phase Transition

The verification of what lies behind VO_2's MIT is difficult since the structural and electronic transitions take place almost simultaneously. Regarding evidence from phonon softening at the high-symmetry R point obtained from DFT+U, it can be concluded that the Peierls and Mott mechanisms associate with one another in delivering the MIT. To elucidate, the Peierls transition is related to the phonon softening instability which is, in turn, believed to bring about the structural transition of VO_2. Phonon dispersions in VO_2 were realized based on DFT and DFT+U, then the results were compared. It turned out that the normal modes at R point derived from DFT+U are in accordance with the V-V distortions, confirming the role of electronic correlations in the Peierls transition. Moreover, decoupling of the structural and electronic transitions was achieved, together with the revelation of a monoclinic-like metallic phase.[15] This unusual monoclinic-like metallic phase is very significant, as it can be interpreted into 2 different scenarios. One assumption involves V-V's spontaneous breaking or substantial weakening in the M1 phase, while another ensures the leading role of the Mott mechanism.

2.3 Graphene

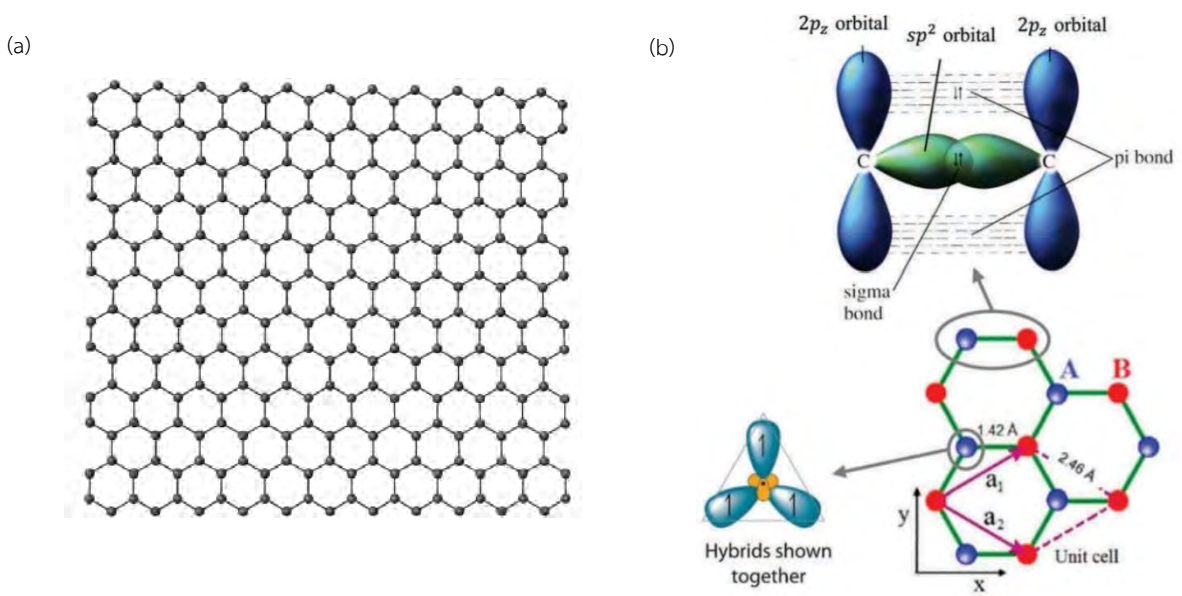

Fig 9. (a) Graphene's honeycomb structure.[16] (b) The unit cell and sp^2 bond of graphene. Red and blue atoms highlight different sublattices.[17]

Graphene is a 2-D honeycomb structure of carbon atoms. The unit cell is not the hexagon itself, but the parallelogram which consists of 2 unequal carbon atoms from different sublattices, namely sublattices A and B. The lattice parameter is the same for both sublattices, of 2.46 Å. Given that the electron configuration of carbon is [He] $2s^2$ $2p^2$, 3 of the valence electrons would form in-plane sigma bonds with its neighbors via

sp^2 hybridization. The sigma bond length or the interatomic distance between carbon atoms is approximately 1.42 Å, hence the stability and the mechanical strength of graphene. The fourth electron in an out-of-plane p_z orbital, on the contrary, would form pi bonds with its adjacent counterparts and allows Van der Waals interaction to take place between each graphene layer or graphene and its substrate. Interestingly, it is this pi bonding which is responsible for the excellent electrical conduction of this 2-D material.[16-18]

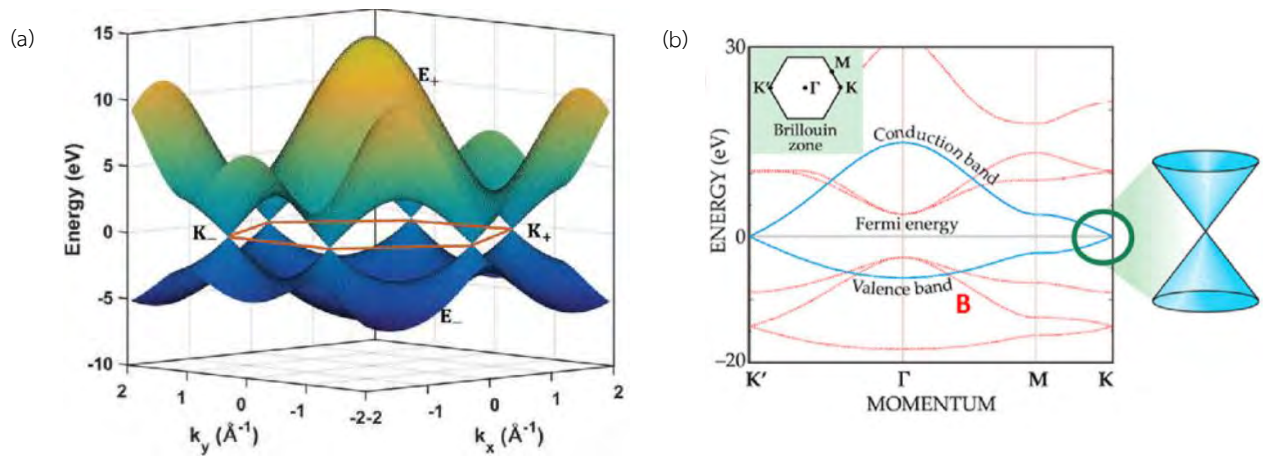

Fig 10. The energy band diagram of graphene (a) as a function of both k_x and k_y. The orange line indicates the boundaries of the hexagonal first Brillouin zone.[17] (b) along some high-symmetry points. The inserted diagram on the top shows the first Brillouin zone of graphene. [19]

Since only the $2p_z$ orbitals involve directly with conduction electrons, a calculation of graphene's electronic band diagram would mainly focus on these $2p_z$ overlaps and employ $2p_z$ orbitals as a basis set of the wavefunction. The method used to derive the band structure is the tight-binding approach with the nearest-neighbor approximation. As a result, the dispersion relation is obtained as in Fig 10. The 2 upper and lower energy bands, called π^* and π bands respectively, originate from the hopping between the equivalent sublattices A and B. Due to the fact that there are 2 conduction electrons per unit cell, the π band is completely filled and the Fermi energy at 0 K lies at the energy of the **K** and **K′** points. Therefore, graphene is a zero-bandgap semiconductor with no available density of states on the Fermi level. Furthermore, looking closely at the energy dispersion near the conduction-valence intersection known as the Dirac point (the blue conical in Fig 10.(b)), it turns out that the dispersion is linear and the electrons mimic Dirac fermions. The Hamiltonian is Dirac-like,

$$H = -i\hbar v_F \boldsymbol{\sigma} \cdot \boldsymbol{\nabla} \tag{3}$$

where $v_F \approx 10^6$ m/s is the Fermi velocity and $\boldsymbol{\sigma} = (\sigma_x, \sigma_y)$ are the Pauli matrices. The electrons behave as if they are massless relativistic particles with an effective speed of light v_F. Unlike electrons from other

conventional metals and semiconductors of which dispersion relation is approximately parabolic, the linear spectrum of 2-D Dirac fermions is the source of astonishing quantum electrodynamics phenomena such as quantum Hall effects, Klein tunneling paradox, and chirality.[16-19]

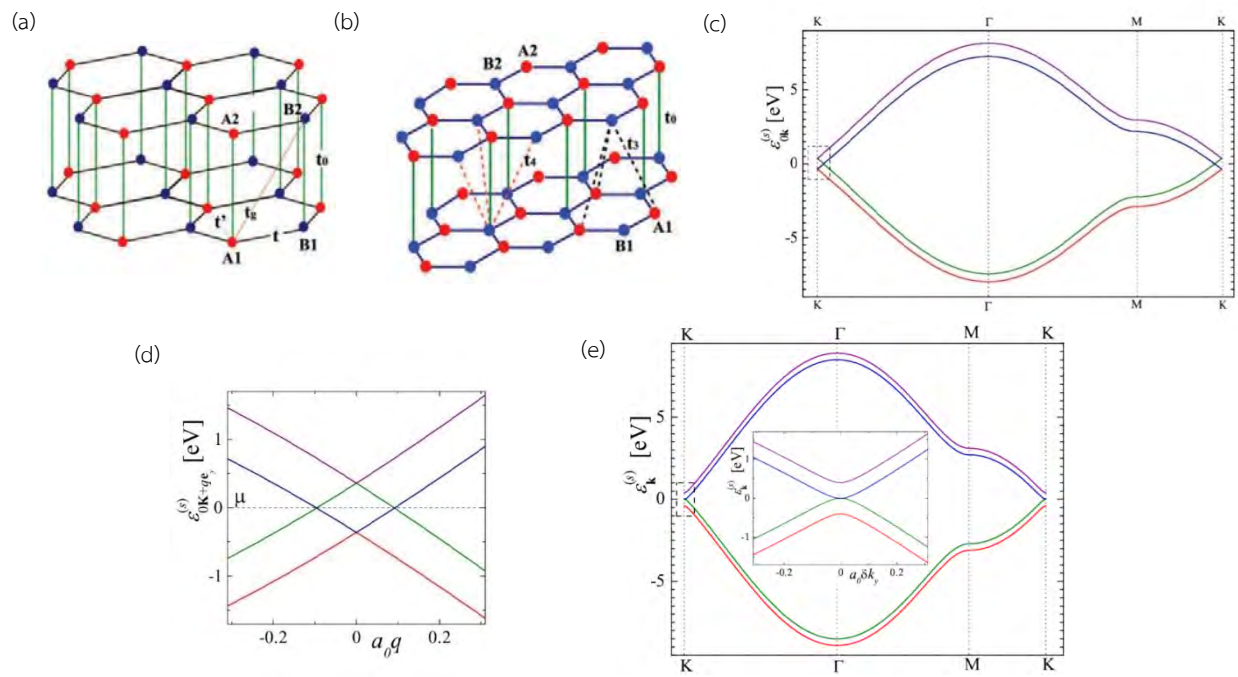

Fig 11. Bilayer graphene in (a) AA-stacked and (b) AB-stacked order.[17] The energy band diagram at Dirac points of (c) AA-stacked and (d) AB-stacked bilayer graphene.[20]

The term graphene can also be reserved for bilayer graphene which is worth investigating in its own right. Bilayer-graphene stacking exists in 2 manners: hexagonal or AA stacking, and more stable Bernal or AB stacking. While each carbon atom just sits on top of its corresponding atom in AA stacking, the AB-stacking layers are rotated 60° relative to each other about an axis perpendicular to the plane and B-sublattice atoms are located above the hexagonal holes of the first layer. Both configurations contain 4 carbon atoms per unit cell. Obviously, distinct stacking orders greatly influence the interlayer-hopping nature of electrons and the dispersion relations. For AA stacking, electrons mostly hop between A1-A2 sites and B1-B2 sites in Fig 11.(a). On the contrary, the interplane hopping varies widely for AB stacking as seen in Fig 11.(b): it can happen between A2-B1 dimer sites, a non-dimer site to nearest non-dimer sites, or a dimer site to nearest non-dimer sites. The resulting band diagrams obtained via tight-binding approach and the nearest neighbor approximation are shown in Fig 11.(c), (d) and (e). Although the general features at large energy might appear the same for both stacking orders, the subtle structures are very different. The AA-stacked band diagram near Fermi level comprises the double monolayer spectra, shifted in opposite direction by the same units. In the vicinity of the Dirac points, the linear energy dispersion is preserved with the same Fermi velocity as that of

the monolayer. The hole-like and the electron-like bands coincide at the Fermi surface (Fig 11.(d)); in other words, the AA-stacked bilayer is metal. Contrarily, for AB stacking, only two bands touch perfectly at the Fermi level. At low energy, the dispersion is no longer Dirac-like but parabolic of that normal Schrödinger formalism.[20-22]

Monolayer and bilayer graphene exhibit fairly similar properties. For any micromechanically deposited graphene, the electron mobility at room temperature is extremely high, exceeding 2000 $cm^2/V.s$. Suffering from the inhibited carrier mobility, the electrical conductivity is lowered as the layer number increases. The thermal conductivity of graphene can reach about 2800 W/m.K. In terms of the mechanical strength of a defect-free sheet, it possesses stiffness of the order of 300–400 N/m with a breaking strength of ~42 N/m. Its Young's modulus is approximately 0.5–1.0 TPa which is about an accepted value for bulk graphite. It is found that these mechanical properties of graphene tend to be affected by temperature changes rather than the layer numbers and isotope substitutions. In addition, thanks to the interaction between light and Dirac fermions, it is very transparent with decreasing transparency as the layer number grows. Regarding all these outstanding properties, graphene offers a wide range of applications in field-effect transistor devices, mechanical reinforcement, and optoelectronic devices like solar cells and touch screens.[18]

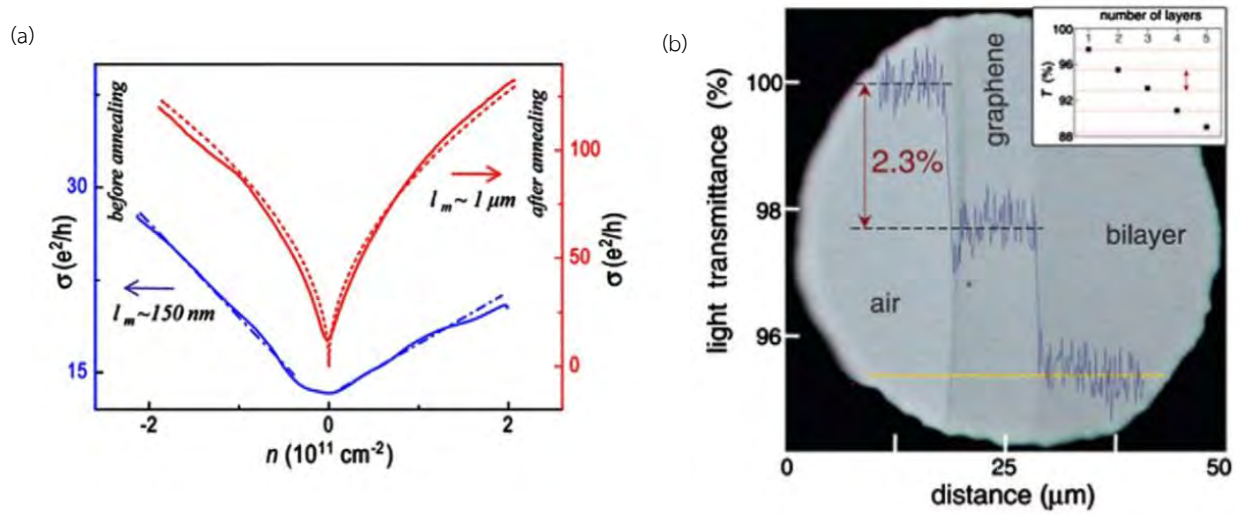

Fig 12. (a) The conductance of a suspended graphene sample at 40 K as a function of carrier density. The blue and red lines represent the sample before and after annealing respectively. (b) The optical transmittance at 550 nm of monolayer and bilayer graphene. The inserted graph shows the variation of the transparency with respect to number of layers.[18]

2.4 Hybridization of VO_2 and Graphene

Despite the potential benefits of VO_2, some of its properties hinder practical applications. It is obvious that T_{MIT} of bulk VO_2 is too high for room-temperature-related devices. On top of that, the visible transmittance is too low and the modulation of solar energy is not efficient enough for use in architecture. Referring back to Fig 2.(a), as the transmittance in the visible spectrum remains almost unchanged, the solar modulation in VO_2 mainly relies on the transmittance difference in the near-infrared region which only constitutes 43% of solar energy in the solar spectrum.[3] Therefore, considering the advantages of both VO_2 and graphene, it is expected that graphene/VO_2 hybrid film would improve the electrical conductivity and the luminous transmittance. For flexible thermochromic windows and architectural adaptations, graphene can also serve as a flexible-yet-firm base of VO_2 and optimize the optical quality of the hybrid film.

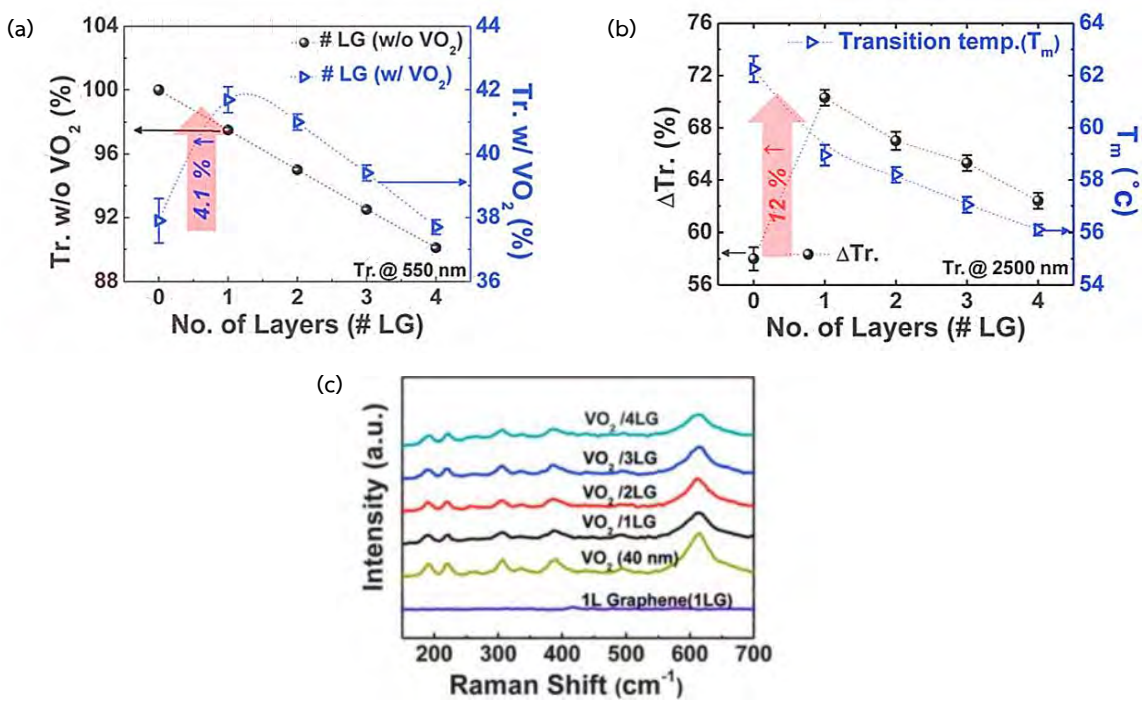

Fig 13. (a) Transmittance at 550 nm of graphene-laminated (black dots) and VO_2/graphene(0–4 layers)/Al_2O_3 (blue dots) (b) Transmittance at 2500 nm and transition temperature of VO_2/graphene(0–4 layers)/Al_2O_3, and (c) Raman spectra in the range of 100–700 cm^{-1} (excited by 532 nm laser) of graphene (1 layer) and VO_2/graphene(0–4 layers) films on sapphire substrates[23]

To this day, there have been several studies regarding the hybridization of these two materials for optimized functionalities. In Enhanced Optical Response of Hybridized VO_2/graphene Films research by Kim et al., a large scale VO_2/graphene/Al_2O_3 was synthesized via chemical vapor deposition (CVD), magnetron sputtering and post annealing.[23] The optical properties of the films were then characterized as a function of the number of graphene layers and temperature. The transmittance of VO_2/graphene(1 layer) at 550 nm was

~4.1%, higher than that of bare VO_2/Al_2O_3 (Figure 13.(a)). In the infrared range at room temperature, there were an increase in the optical transmittance of VO_2/graphene(1-4 layers)/Al_2O_3 and a decrease in its T_{MIT} (Figure 2b). It was believed that the lower T_{MIT} derived from surface strain: negative-thermal-expansion graphene versus positive-thermal-expansion sapphire substrate and VO_2. The amount of surface strain was proportional to the number of graphene layers, meaning T_{MIT} of VO_2 could be further lowered down to some level. In the range of 100–700 cm^{-1}, VO_2/graphene(1-4 layers)/Al_2O_3 exhibited well-defined typical Raman spectra which were absent for the graphene-only sample (Figure 13.(c)). Moreover, x-ray diffractometer (XRD) was applied to analyze the structure of the hybridized films. The result showed that VO_2 films on bare sapphire substrates possessed a significant peak of (020) plane with a minute (002) plane (Figure 14.(a)), while there was a mixed phase with (200), (020), and (011) planes for VO_2/graphene(1-4 layers)/Al_2O_3 (Figure 14.(b)).

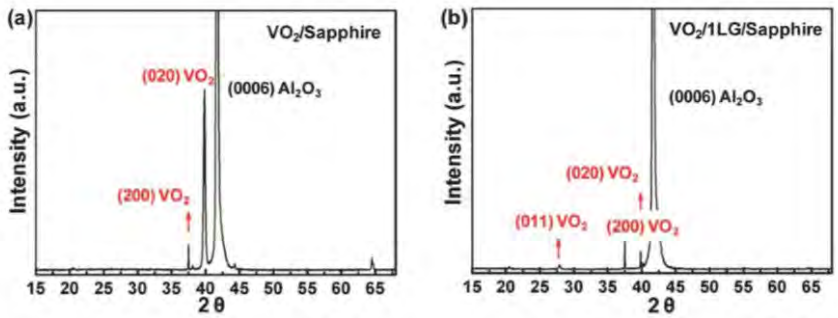

Figure 14. XRD analysis of (a) VO_2/Al_2O_3 and (b) VO_2/graphene/Al_2O_3[23]

Another research by Kim et al., Flexible Thermochromic Window Based on Hybridized VO_2/Graphene, followed the same preparation procedure as the above VO_2/graphene/Al_2O_3 but with Al_2O_3 replaced by Cu.[24] To create flexibility of VO_2 film for energy-sufficient smart windows, Cu etching process was performed and VO_2/graphene was transferred to PET film. The control experiment of VO_2 transfer to PET film with the absence of graphene revealed failure, hence the importance of graphene in the transfer process. For Raman analysis, both graphene-free (VO_x/Cu) and graphene-supported VO_2 (VO_2/graphene/Cu) showed several peaks corresponding to the characteristic vibration modes assigned to monoclinic VO_2 (Figure 15.(b)). However, the Raman peaks of VO_2/graphene/Cu were much more distinct as compared with those of VO_x/Cu, evidently due to dense VO_2 distribution on the graphene support. Although VO_2/graphene showed a typical Raman feature of CVD-grown graphene, there was a slight increase in the D-peak intensity of graphene after VO_2 formation (Figure 15.(a)). Unfortunately, this peak implied high-temperature oxidation of graphene during post annealing of VO_x at 500 °C under O_2 flowing. As the temperature increased, the characteristic Raman peaks of monoclinic VO_2 diminished through intermediate phase coexistence regimes and then completely disappeared at ~70 °C, indicating a structural transition of the monoclinic phase into the rutile phase. As the

temperature decreased, the monoclinic signature reappeared, showing the reverse transition. Therefore, this VO_2/graphene film confirmed the characteristic of reversible first-order transition.

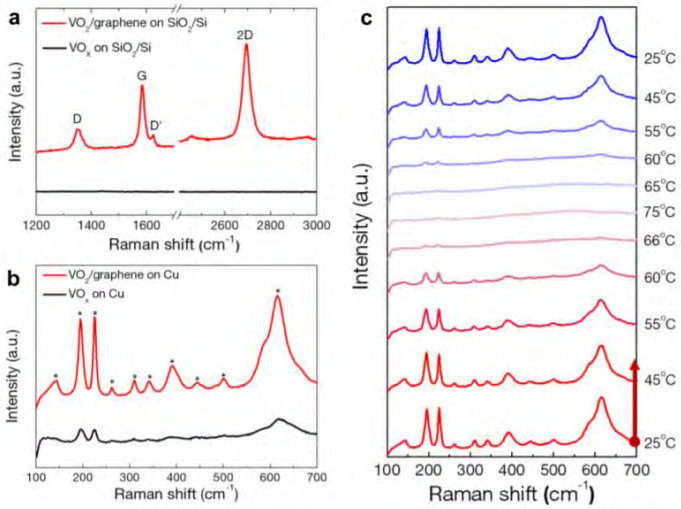

Fig 15. Raman spectral analysis of VO_2/graphene. (a,b) Raman spectra (excited by 532 nm laser) of VO_2/graphene in comparison with graphene-free VO_x. (c) Temperature-dependent Raman spectra of VO_2/graphene[24]

In addition, the hybridization of VO_2/graphene lowered the T_{MIT} to 61 °C. Kim et al. enumerated 2 causes of this phenomenon: the effect of graphene support on reducing VO_2 crystal size to nanoscale and the efficient heat transfer from graphene to VO_2. The fabricated VO_2/graphene films were then integrated into a model house and shown to reduce the in-house temperature efficiently, proving its potential as energy-saving smart window films.

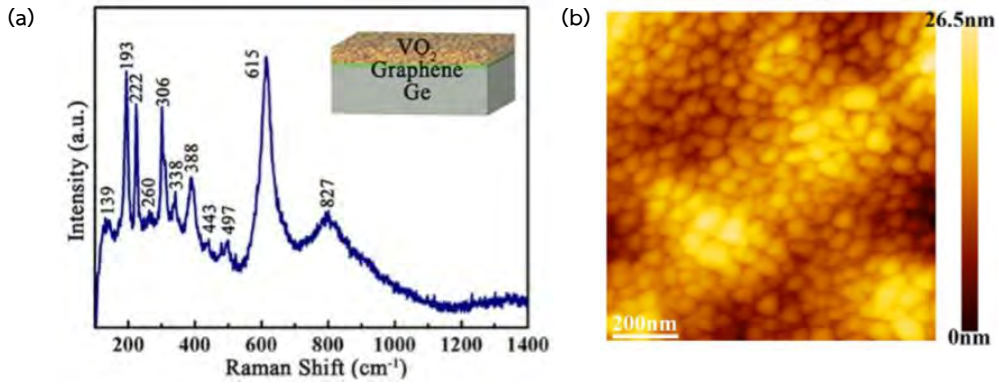

Fig 16. (a) Raman spectral analysis of VO_2/graphene/Ge and (b) Surface topography of VO_2/graphene/Ge by AFM[25]

In Electron Transfer Induced Thermochromism in a VO_2–Graphene–Ge Heterostructure by Zhou et al., VO_2/graphene/Ge hybrid was prepared by reactive sputtering and atmospheric pressure chemical vapor deposition (APCVD).[25] For characterization, it was observed that almost all known Raman modes of

monoclinic VO_2 were present with no irrelative peaks (Figure 16.(a)). From the XRD result, it was found that the VO_2 film on Graphene/Ge mainly consisted of an amorphous phase. The crystallinity of VO_2 was affected by the atomic-scale wrinkles of graphene, as indicated by AFM (Figure 16.(b)) and HR-TEM. Furthermore, the T_{MIT} of VO_2/graphene/Ge appeared to be ~330 K which was lower than that of VO_2 films on Ge substrate. Apart from the contribution of differences in thermal coefficient between interlayers, Zhou et al. also introduced the mechanism of electron injection and doping facilitated by graphene. The electron transfer could increase the electron density in VO_2 film, destabilize the semiconductor phase, and thus decrease the T_{MIT} of VO_2 film.

From these studies, it is evident that a different attempt is required to approach VO_2 – graphene hybridized film. In other words, the post-annealing process to obtain VO_2 on graphene leads to the oxidation of graphene, which in turn decreases the film efficiency. VO_2 grown on graphene might also turn up as an amorphous phase, exhibiting poor crystallization quality due to the atomic-scale wrinkles of graphene.

2.5 Raman Spectroscopy

Raman spectroscopy is one of general tools used to explore crystal vibrations and structures. The whole process involves a monochromatic continuous-wave laser irradiating a material, and the detection of a relatively weak signal of inelastic scattering of the incident light, called Raman scattering. Generally, a light wave can be thought of as a propagating oscillating dipole of which size is usually much larger than a molecule (within visible spectrum limit). This dipole then causes distortion of electron cloud or electric polarization, forming a very short-lived intermediate state from which the photon is emitted immediately. Actually, there are 2 possible scenarios concerning nuclear movement which result in different scatterings. If only electron cloud distortion is involved in scattering, the photons are scattered with very small frequency changes, as the electrons are light compared with the atomic nucleus. This elastic scattering, named Rayleigh scattering, occurs predominantly in the process. On the other hand, if nuclear motion is induced during scattering, energy is transferred either from the incident photon to the molecule or from the molecule to the scattered photon. In these cases, the process is inelastic and the energy of the scattered photon is different from that of the incident photon by principally one vibrational unit. This is the Raman scattering. It is inherently a weak process in that only one in every 106 –108 scattered photons is Raman scattered. A Raman spectrum is defined by the intensity of the inelastically scattered light as a function of energy loss from the incident light. The energy loss is called the Raman shift, usually given in units of cm^{-1} (1 eV = 8,065 cm^{-1}).[26]

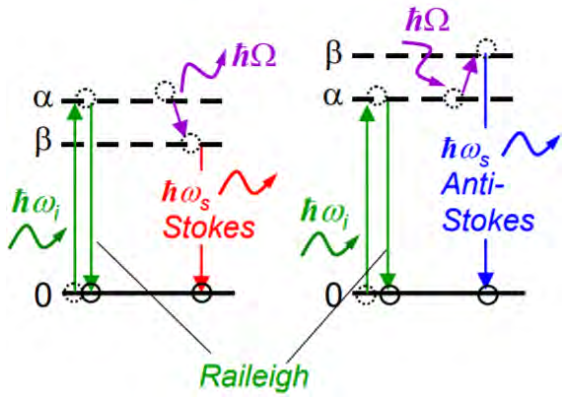

Fig 17. A schematic diagram of the first-order Raman scattering. ω_i, ω_s, and Ω are the frequencies of the radiating field, the scattering photon, and the scattering phonon respectively.[27]

The induced nuclear motion mentioned above is, in fact, related to phonon creation or phonon absorption. At non-zero temperatures, the atoms in crystals vibrate about some equilibrium position. The complex vibrations of the lattices in 3 dimensions are a combination of 3N normal modes where N is the number of atoms in a unit cell. Moreover, the energy of each normal mode is restricted to integer multiples of a quantum of energy called a phonon.[28] In first-order Raman scattering, there are three fundamental sub-processes as shown in Fig 17. Beginning with the photon absorption, an electron is excited from an initial state (an occupied electronic state) to the first intermediate state (depicted by $\boldsymbol{\alpha}$ in Fig 17.). Next, the photoexcited electron either emits a phonon by losing one phonon energy (Stokes Raman scattering) or absorbs a phonon (anti-Stokes Raman scattering), and goes to the second intermediate state (depicted by $\boldsymbol{\beta}$ in Fig 17.). Culminating in electron-hole combination, a photon is emitted as inelastically scattered light. The two intermediate states can either be a real electronic state or a virtual state, which is a linear combination of excited states. If one of the two intermediate states is the real state, the Raman intensity is enhanced. In this case, it is called the resonance Raman scattering which is actually what happens in graphene. For second-order Raman scattering, there is one more intermediate state added, and 2 phonons are released.[29]

The scattering has to obey the energy and momentum conservation rules in (4) and (5).

$$\hbar\omega_s = \hbar\omega_i \pm \hbar\omega_k \tag{4}$$

$$\hbar\boldsymbol{k_s} = \hbar\boldsymbol{k_i} \pm \hbar(\boldsymbol{q_k} + \boldsymbol{G}) \tag{5}$$

The variables $\omega_s(\boldsymbol{k_s})$, $\omega_i(\boldsymbol{k_i})$, and $\omega_k(\boldsymbol{q_k})$ correspond to the frequencies (wavevectors) of the scattered light, the incident light, and the phonon respectively. The term $\hbar\boldsymbol{G}$ represents the crystal momentum which takes any values from a set of reciprocal lattice vectors. Since the wavevectors of the incident and scattered

photons are approximately the same within the range of 10^4 -10^5 cm^{-1} which are much smaller than the size of the Brillouin zone, $\boldsymbol{G}$ must be chosen zero to fulfill (5).[30] Thus, only the phonon modes with wavevectors $\mathbf{q} \sim 0$ (Γ point) are allowed in the first-order Raman scattering. Contrarily, since there are 2 phonons present in the second-order Raman scattering, possible wavevectors can be extended to the whole Brillouin zone as long as the sum of the two phonons' wavevectors participating is zero: $\mathbf{q}_1+\mathbf{q}_2 \sim 0$.[31]

Despite following energy and momentum conservation rules, not every vibrational mode is Raman active mode, which is the one that appears on Raman spectra. There is a selection rule requiring that the Raman active modes are those that cause a change in the polarizability of the electron cloud. The polarizability is a measure of the degree to which the electrons in the molecule can be displaced relative to the nuclei. It is an anisotropic property, thus represented by a rank-2 tensor.[32] The polarizability $\boldsymbol{\alpha}$ is related to an induced electric dipole $\boldsymbol{\mu}$ and the irradiating electric field $\boldsymbol{E}$ as follows:

$$\boldsymbol{\mu} = \alpha \boldsymbol{E} \tag{6}$$

Moreover, $\boldsymbol{\alpha}$ can be expressed as a Taylor series expansion, and the magnitude of $\boldsymbol{E}$ and a normal coordinate $\boldsymbol{Q}$ can be written as

$$\alpha = \alpha_0 + \left.\frac{d\alpha}{dx}\right|_0 x + higher\ terms \tag{7}$$

$$E = E_0 cos(2\pi\omega_0 t) \tag{8}$$

$$Q = Q_0 cos(2\pi\omega_v t) \tag{9}$$

where $\boldsymbol{x}$ is a vibrational displacement, E_0 is the electric field's amplitude, Q_0 is the normal mode's amplitude, ω_0 is the radiation frequency, and ω_v is the normal mode frequency. For each normal coordinate Q, $\boldsymbol{\mu}$ in (6) then becomes

$$\mu = \alpha_0 E_0 cos(2\pi\omega_0 t) + \frac{1}{2}\left.\frac{d\alpha}{dQ}\right|_0 Q_0 E_0 [cos(2\pi(\omega_0 - \omega_v)t) - cos(2\pi(\omega_0 + \omega_v)t)] + \cdots \tag{10}$$

The first term in (10) corresponds to the Rayleigh scattering, and the second term belongs to the Raman scattering. Now, it is the second term that determines the active mode condition. The fact is that intensities of the Raman transitions are proportional to the absolute square of a vibrational Raman transition moment $\boldsymbol{R}$ between states with wavefunctions ψ' and ψ, which can be calculated from the electric dipole:

$$\boldsymbol{R} = \int \psi' \boldsymbol{\mu} \psi \, dx \tag{11}$$

Substituting (8) into (9), it can be found that the intensity I is proportional to

$$I \propto |\boldsymbol{R}|^2 \propto \left(\frac{d\alpha}{dQ}\Big|_0\right)^2 \tag{12}$$

This relation is simply in agreement with the selection rule stated earlier. It should be noted that the Raman process relies heavily on the chosen frequency of the laser, as it defines the energy of the intermediate state and the extent of the distortion or the polarizability.[32,33]

2.5.1 Raman shifts of VO_2

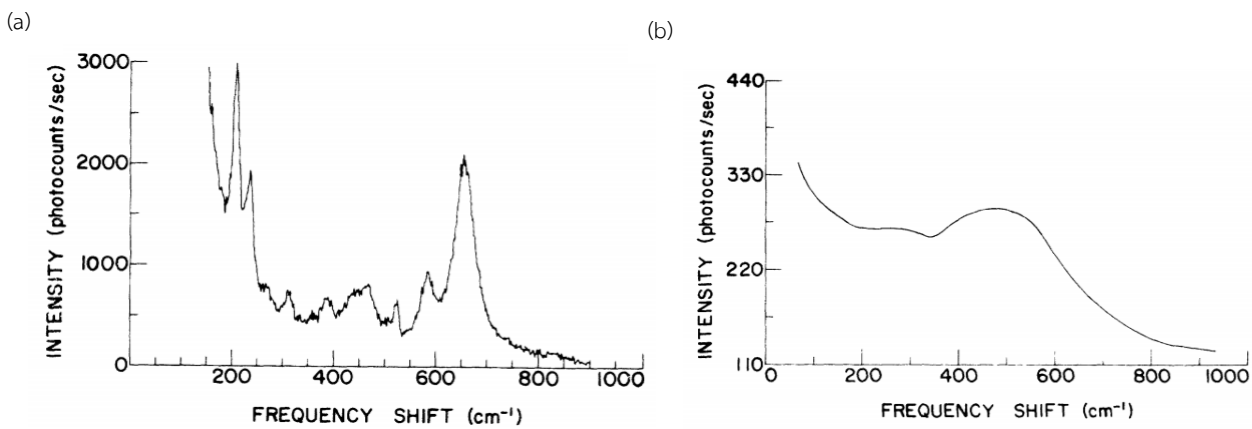

Fig 18. Unpolarized Raman spectra of VO_2 at (a) 300 K (M1 phase) and (b) 375 K (R phase).[34]

Raman scattering has been favoured to explore lattice vibrations and SPT in VO_2 since the large incoherent cross section of vanadium and the free-carrier absorption in the metallic phase prohibit inelastic neutron-scattering and infrared measurements.[34] Based on a group theoretical analysis, the active Raman modes of VO_2 can be predicted. The space groups of R-VO_2 and M1-VO_2 are $\mathbf{D_{4h}^{14}}$ and $\mathbf{C_{2h}^{5}}$ respectively.[1] Theoretically, 4 active modes of A_{1g}, B_{1g}, B_{2g}, and E_g are present in the R phase, while 9 A_g and 9 B_g active modes should be observed in the M1 phase. However, as seen in Fig 19.(b), it turns out that one B_g mode is absent in the M1 phase.[35]

For R-VO_2, its Raman spectrum is usually compared with that of TiO_2. Although they both possess similar rutile structure and the equivalent numbers of the active modes, the Raman spectrum of TiO_2 is much more discernible with stronger and sharper Raman bands. As reported in Fig 18.(b), the Raman spectrum of R-VO_2 consists of several weak and broad lines with a strong fluorescence background.[34] Since the mode at 510 cm^{-1} showed a strong polarization dependence, it was assigned to the A_{1g} symmetry.[36] All of these 4 modes are associated with the motion of the oxygen atoms only. The E_g mode demonstrates the motion along the c_r axis of the cell-face oxygen atoms. The motions of the A_{1g} and B_{2g} modes are in the ab-plane towards the

axis of symmetry parallel to c_r axis. Nonetheless, all atomic pairs move in-phase for B_{2g}, whereas for A_{1g}, the central pair moves of phase. For B_{1g}, vibration still occurs in the ab-plane but in the direction perpendicular to B_{2g}.

On the contrary, the M1 phase exhibits a set of strong well-resolved Raman bands. Polarized Raman measurements on epitaxial M1-VO_2 films could determine the symmetries of all the experimentally observed Raman modes, as depicted in Fig 18.(a). Unfortunately, A_g and B_g lines are found coexisting near 224 and 393 cm^{-1} as they have not been resolved experimentally. The missing ninth B_g mode is probably located at 450 cm^{-1}. The B_g modes are usually weak in Raman intensity. The modes in the high energy region like 612 cm^{-1} (or 618 cm^{-1} in some research) can be related to the stretching mode of V-O vibration, while those in the intermediate energy range are ascribed to be associated with the different bending modes of V-O vibration. For the low-energy modes like ~194 and ~224 cm^{-1}, they are assigned to V-V vibration. [30]

(a)

Raman shifts (cm^{-1})	Phonon modes
137	A_g
143	B_g
194	A_g
224	A_g , B_g
262	B_g
310	A_g
340	A_g
393	A_g , B_g
442	B_g
484	B_g
499	A_g
582	B_g
612	A_g
663	A_g
820	B_g

(b)

Raman shifts (cm^{-1})	Phonon modes
240	-
390	-
510	A_{1g}
625	-

Fig 19. Raman shifts and corresponding active phonon modes of (a) M1-phase and (b) R-phase VO_2.[35]

Temperature-dependent Raman spectroscopy has long been used to investigate phase change at different temperatures and the insight into SPT. According to Huang et al., the temperature-dependent Raman

peaks of VO_2/ZnO films were observed as shown in Fig 20. (a). It can be seen there was a strong dependence of Raman resonance peaks intensity on temperature: the amount of the phonon modes related to the resonance peaks decreased together with the scattering peak intensity. It was assumed that there were 2 factors regarding the disappearance of the Raman modes at high temperature, which were the symmetric stretching of V-O-V bond in the tetragonal phase and the increasing of free carrier absorption. Furthermore, temperature-dependent Raman peak shifting was observed, presumably the transition into different VO_2 phases. As depicted in Fig 20.(b), the low-energy mode at 192 cm^{-1} and high-energy mode at 613 cm^{-1} experienced red and blue shifts respectively.[37]

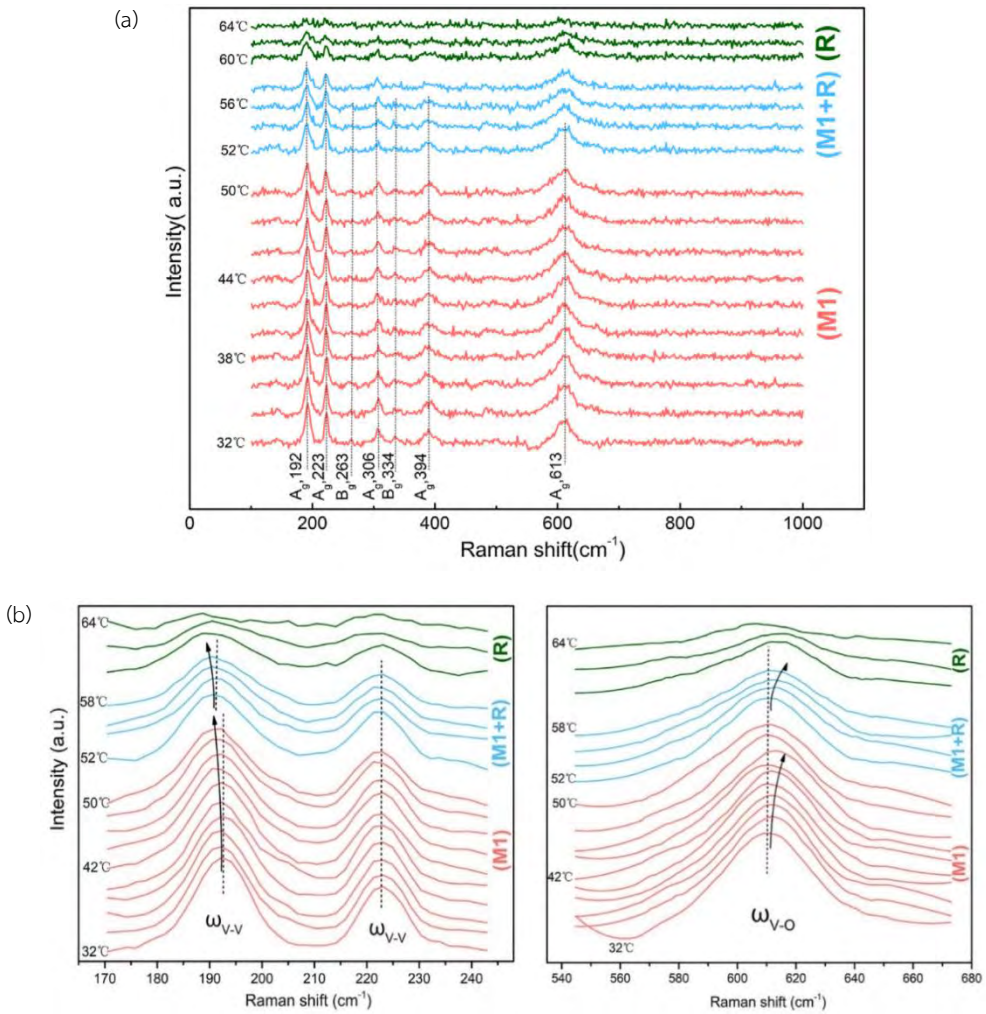

Fig 20. Temperature-dependent Raman shifts of VO_2/ZnO for (a) all observed modes and (b) modes at 192, 223 and 613 cm^{-1}.[37]

In addition, research on VO_2/Al_2O_3 with different orientations of Al_2O_3 by Nazari et al. yielded the same characteristic temperature-dependent peak shifting. In Fig 21., starting at room temperature, it was found that VO_2's phonon energies depended on the substrate orientation. The blue shift of 615 cm^{-1} mode

was deemed a consequence of the tensile stress parallel to the sapphire substrate plane, which produced compressive strain in the growth direction. In contrast, strain has a weaker effect on the other Raman bands. Besides, the tensile strain along the c_r direction in VO_2/c-Al_2O_3 caused the V-V vibrations to red shift as seen at 195, 224, and 309 cm^{-1} bands. For VO_2/m-Al_2O_3, the 262 and 615 cm^{-1} vibrations gradually red shifted, while there was just a slight red shift for VO_2/r-Al_2O_3. Normally, strain in these samples had been anticipated to arise from lattice-constant mismatches with the substrate and thermal stresses due to the different expansion coefficients between 2 materials. In the case of VO_2 and Al_2O_3, VO_2 has a much larger thermal expansion coefficient than that of Al_2O_3, especially in the c_r direction. However, it was discovered that if the strain origin solely relied on these factors, the red shift of the low-energy bands of VO_2/c-Al_2O_3 would be unexplainable. In fact, gradual blue shifts from the whole set of 615, 224, and 195 cm^{-1} modes in VO_2/c-Al_2O_3 had been reported when tensile stress was applied along the c_r direction as VO_2 transformed from M1 to M2 at room temperature. To explain the phenomenon, the effect of internal stresses in the M1-VO_2 during the phase transition was introduced. These stresses were produced by the neighboring regions which had transformed in the intermediate temperature range. Partial transformation from M1 to M2 would produce compressive stress on the untransformed regions of M1-phase VO_2. This internal stress would increase with transformed volume fraction to steadily blue shift the V-O vibrations with increasing M2 volume fraction. The obtained blue shift of the 615 cm^{-1} band was in agreement with the computed value of 4-6 cm^{-1} via Young's modulus of VO_2 and pressure dependence of 615 cm^{-1} phonon. For the case where VO_2 transformed directly from M1 to R phase, the V-O vibrations would be red shifted due to the contraction along the c_r axis, as can be seen from VO_2/m-Al_2O_3. The impact of these internal strains was not pronounced in the case of 195 and 224 cm^{-1} bands owing to their weak pressure coefficients. Furthermore, it became clear that the stress induced by thermal expansion mismatch with the substrate was nearly one order of magnitude smaller than the internal stresses, implying its irrelevance.[38]

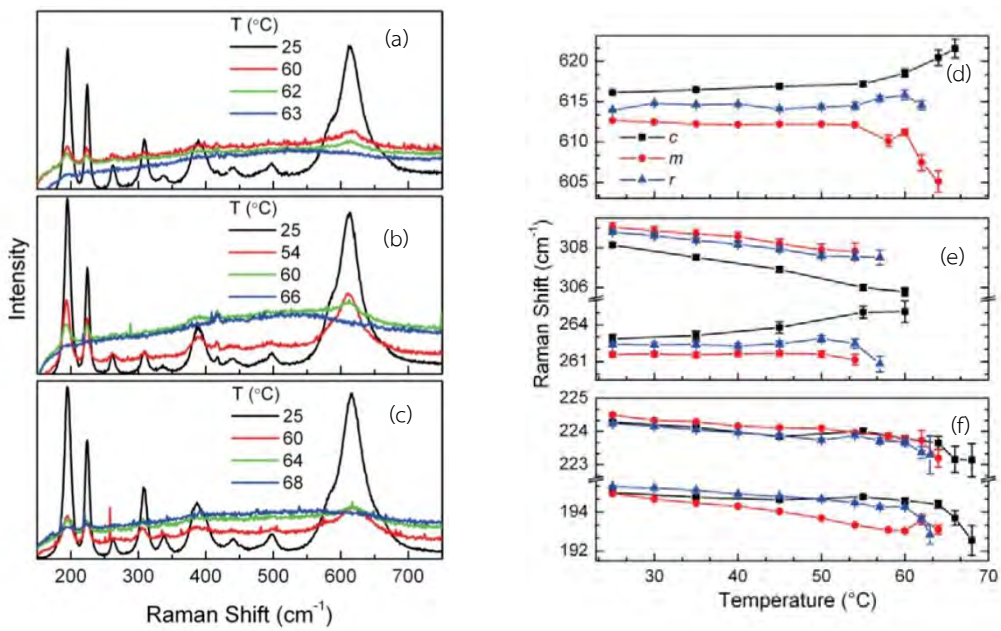

Fig 21. Temperature-dependent Raman shifts of VO_2/Al_2O_3 having different crystal orientations (a) r-Al_2O_3, (b) m-Al_2O_3, and (c) c-Al_2O_3. Phonon energies as a function of temperature at (d) 615 cm^{-1}, (e) 263 and 309 cm^{-1}, and (f) 195 and 225 cm^{-1}.[38]

2.5.2 Raman shifts of Graphene

Raman spectroscopy has been prominently chosen as a characterization tool for carbon family owing to nondestructive inspection and extensive coverage of structural and electronic features. In order to understand Raman features of graphene, its phonon dispersion is firstly considered.

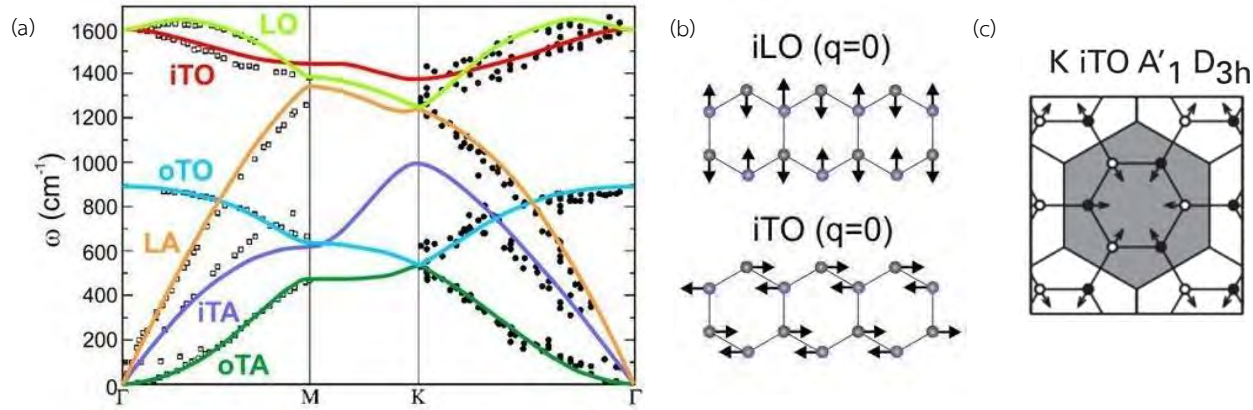

Fig 22. (a) Phonon dispersion relation of graphene along the high-symmetry points Eigenvectors of (b) iLO and iTO phonons at Γ point[39] and (c) iTO phonon at K point[40]

For the sake of simplicity, phonon modes and Raman shifts which are related to crystal defect would be omitted. Since the number of phonon branches is 3N where N is the number of atoms in a unit cell,

graphene has a total of 6 phonon branches. Among these branches, 3 of them are acoustic, meaning each pair of sublattices has an in-phase coordination. The other 3 branches are optical with an out-of-phase movement of the 2 sublattices.

As a result of the peculiar dispersion of the π electrons in graphene, the Raman scattering is always resonant. For the first-order Raman scattering, Raman-active modes at Γ are analyzed with the point group D_{6h}. It turns out that Raman-active modes in general D_{6h} are in-plane doubly degenerate (E_{2g}) or out-of-plane nondegenerate phonon modes (A_g). However, in monolayer graphene, the A_g mode is not present and there are, in fact, 2 groups of E_{2g}. The acoustic E_{2g} of the longitudinal acoustic (LA) and the in-plane transversal acoustic (iTA) modes has no Raman shift. Therefore, the only first-order Raman-active mode of graphene is that of another E_{2g}, the degenerate in-plane longitudinal optical (iLO) and in-plane transversal optical (iTO). This active mode, called G-band, can be observed at ~1585 cm^{-1} in graphene's Raman spectrum. The G-band is a common Raman feature of sp^2 carbon materials with varying scattering intensities and widths. The relatively high frequency of the G-band optical phonon (~0.2 eV) enables Raman spectroscopy to examine perturbations in graphene such as variations in strain, doping, and temperature.[29,39-41]

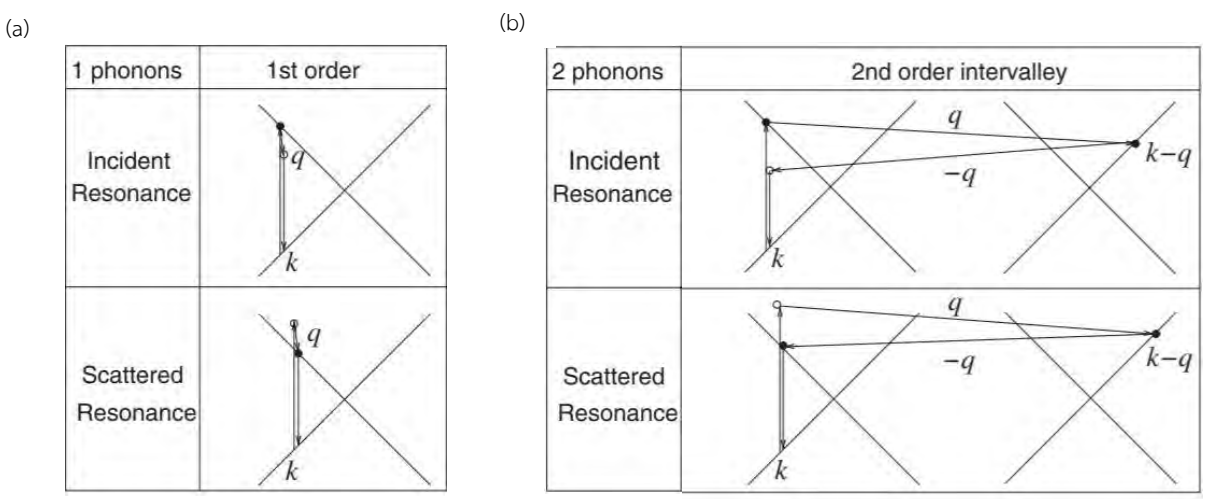

Fig 23. The resonance Raman scattering of graphene. The depicted band diagram is in the vicinity of graphene's valleys. The solid and open circles represent real and virtual electronic states respectively. Each scattering order comprises the 2 possible cases of the incident and scattered resonances. (a) The first-order Raman scattering. (b) The second-order Raman scattering.[29]

In the matter of the second-order Raman scattering, another Raman-active mode of iTO branch near the K point called G′-band (or 2D-band) arises as a result of double resonance Raman scattering. In this process, the photoexcited electron emits 2 phonons before recombining with the hole. As seen in Fig 23.(b), there are now 3 intermediates state, and the term 'double resonance' simply signifies that 2 of the 3 intermediate states are to be real electronic states. Moreover, as graphene has 2 valleys at the K and K′

points, the phonon wavevector q can be chosen either within the same valley or between the two valleys. For the G′-band, the latter scattering turns out to be the case. [43,44]

For monolayer graphene, the G′-band's intensity is much larger than that of the G-band by virtue of the intense double resonance Raman and the electron-phonon interaction of the iTO mode at the K point. As the number of layers increases, the G-band's intensity becomes dominant, exceeding that of the G′-band. The explanation traces back to the interlayer interaction which splits the energy bands near the Dirac cones, leading to phonon frequency distribution. As a consequence, the G′-band broadens and has relatively low intensity. On the other hand, the G-band's intensity is linearly proportional to the number of layers.

Raman peak shifts can be attributed to weaker C-C bonds and changing double resonance Raman condition. The former is associated with an increase in temperature (phonon anharmonicity) and strain, whereas the latter is related to laser photon energy and the layer number. When there is a temperature rise, the G-band frequency monotonically decreases. With increasing laser energy, the photoexcited electron is excited at a different k state along the electronic energy dispersion of the valence and conduction bands; therefore, the double resonance phonon q vector that connects two intermediate real electronic states alters. Furthermore, the G-band exhibits redshift with the growing layer number due to band transformation.[29] Unlike most materials, FWHM of G-band is predicted to have a net decrease with temperature.[43]

As stated earlier that the G′-band's intensity and linewidth depend significantly on the layer number, the G′-band is regarded as graphene's layer number identification. Fig 24.(a) and (b) show the transformation of the G′-band (2D-band) as the stacking number grows. As opposed to the single sharp 2D-band of graphene, the 2D-band of bulk graphite has 2 components of distinct intensities called $2D_1$ and $2D_2$ (Fig 24.(c)). For bilayer graphene, the 2D-band is composed of 4 peaks of higher-intensity $2D_{1A}$ and $2D_{2A}$, and lower-intensity $2D_{1B}$ and $2D_{2B}$ (Fig 24.(d)). The intensities of $2D_1$ peaks rapidly diminish as more stacks are added. Moreover, these 4 components principally emerge from 2 different mechanisms, namely the splitting of the phonon branches and the splitting of the electronic bands. However, DFT indicates that the effect of phonon-branch splitting is too small for such 2D splitting. It can then be concluded that the origin of this splitting is the 4 electronic bands near the Fermi level of bilayer graphene. As shown in Fig 24.(e), the two almost degenerate phonons can choose to couple any 2 of 4 bands available, hence the 4 Raman peaks of the phonons with different wavevectors q_{1A}, q_{1B}, q_{2A}, and q_{2B}. The $2D_{1A}$ and $2D_{2A}$ peaks are higher than the $2D_{1B}$ and $2D_{2B}$ because the phonons q_{1A} and q_{2A} scatterings are dominant, occurring between bands of the same type. Beyond 5 layers, the 2D-band's characteristic becomes hardly distinguishable from that of bulk graphite.[43,44]

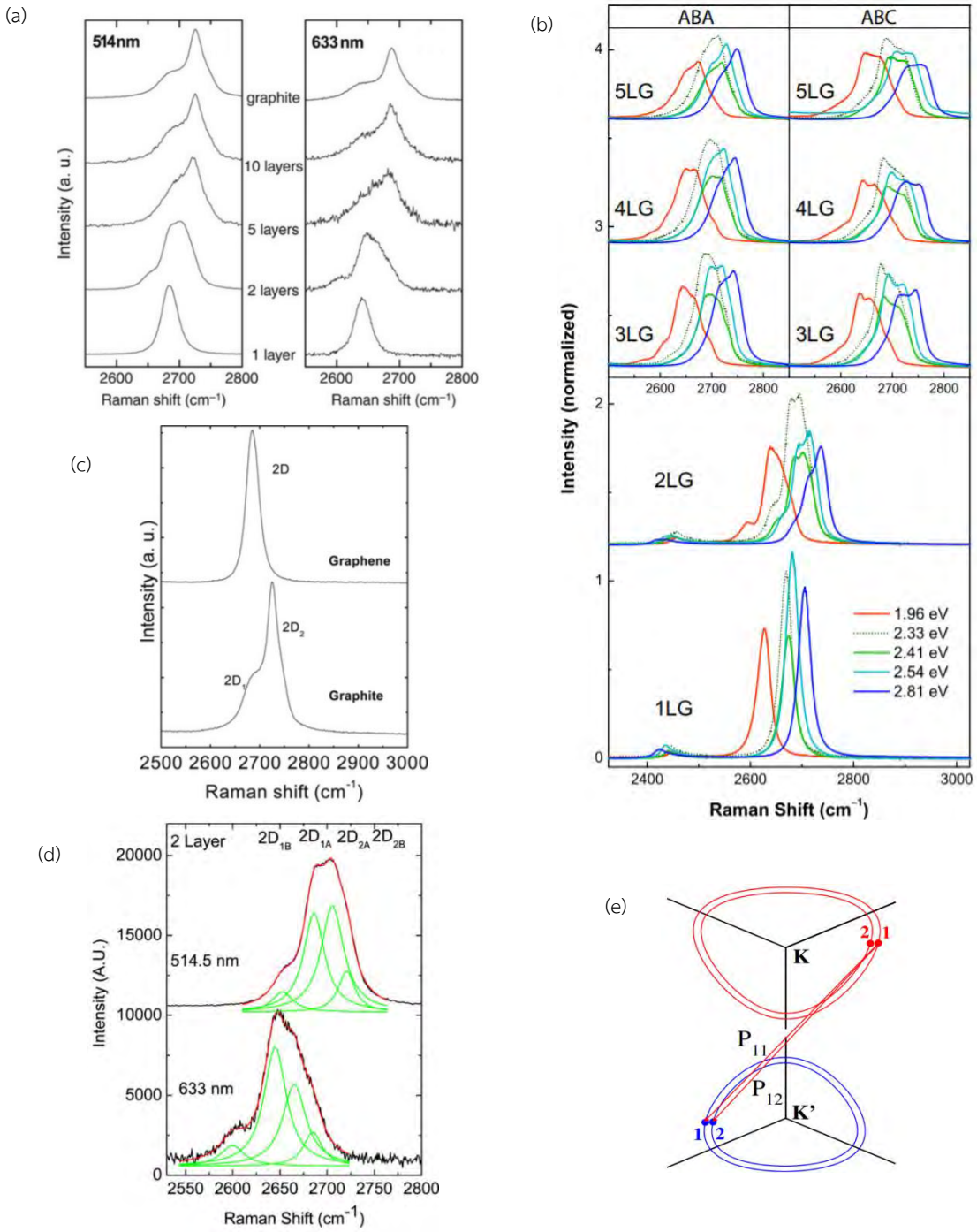

Fig 24. The Raman spectra of the G´-band (2D-band) (a) as a function of the layer numbers for 514 and 633 nm laser[43], (b) as a function of the stacking orders, the layer numbers, and the excitation energy [45], (c) of graphite and graphene, and (d) of bilayer graphene for 514 and 633 nm laser.[43] (e) The 4 possible phonon scatterings near the valleys: 1→1, 1→2, 2→1, and 2→2.[44]

3. Experiments

3.1 VO_2 fabrication

The 50 nm and 100 nm VO_2 on c-Al_2O_3 were previously prepared via reactive bias target ion beam deposition (RBTIBD) at University of Virginia, USA. The c-plane sapphire substrates were chosen since the c-plane contains hexagon lattice corresponding to the hexagonal structure of graphene. As in-plane lattice parameters of VO_2 are larger than those of sapphire, the film growth on sapphire normally has in-plane compressive strain due to substrate clamping effect. The strain would be less in thicker VO_2 film due to strain relaxation.

Illustrated in Fig 25., the process involved a low energy ion source that combines a hollow cathode electron source (HCES) and an end-Hall ion source. The HCES and the end-Hall ion source are powered by a supply with a voltage range 0-100 V and 0-12 A. The HCES is used to eject electrons into the end-Hall ion source. The electrons then interact with the magnetic field near the end-Hall ion source causing ionization of inert gas, and the ionized gas is accelerated using a separate voltage source. Two gas lines, one Ar and one Ar/O_2 mixture, are fed into the chamber through the anode of the ion source, and a third Ar gas line is fed through the HCES. The Ar/O_2 (80/20) mixture is used as the reactive gas instead of pure O_2 to give more control over the flow rate at low concentrations of O_2. The target bias is applied by a pulsed dc voltage source which alternates between a large negative bias (900 V) and a small positive bias (20 V) at a controlled frequency (71.43 Hz) with a 3 μs positive pulse period. Sputtering occurs only during the negative bias pulse period, but not during the positive pulse period or zero bias. The positive bias plays a role in discharging an insulating dielectric of oxygen gas on the target surface, avoiding target poisoning. The positively charged inert gas ions, attracted by this very large potential difference, accelerate toward the vanadium target surface at a near normal incidence angle at high enough energies to induce sputtering. The gaseous vanadium reacts with the oxygen gas to form a VO_2 thin film by condensing onto a substrate.[46,47] (Other growth conditions can be found in ref. [47].)

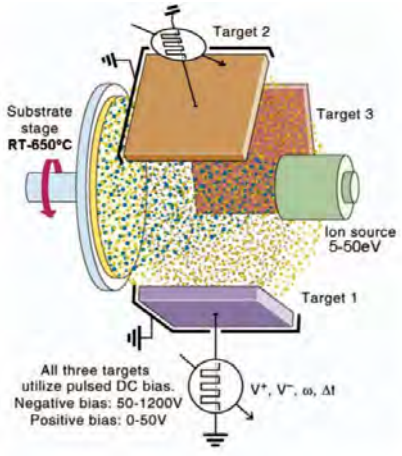

Fig 25. Schematic diagram of RBTIBD growth chamber.[46]

3.2 Resistance vs temperature

To investigate the electrical transition, the resistance data of VO_2/Al_2O_3 was collected using a hotplate and a multimeter (2-point measurement) from 30 to 110 °C with a 5 °C step and maximum uncertainty of ±5 °C. Only the heating up process was involved. The T_{MIT} is the temperature where $\frac{d[\log(\text{Resistance})]}{d(\text{Temperature})}$ is minimum.[47]

3.3 Graphite exfoliation

With an interlayer van der Waals interaction energy of about 2 eV/nm^2, the order of magnitude of the force required to exfoliate graphite is about 300 nN/μm^2. This extremely weak force can be easily achieved with an adhesive tape. The micromechanical exfoliation remains the best method in terms of electrical and structural quality of the obtained graphene, thanks to the high-quality of the starting single crystalline graphite source. However, it is labor intensive and remains unfeasible for a largescale production level.[18]

By sticking and peeling a graphite flake on the tape, several flakes of few-layer graphene (FLG) could be acquired and later transferred onto the VO_2/Al_2O_3 substrate. Aside from the traditional process, the tapes with graphene samples were heated at 100 °C for 2 minutes before they were peeled off from the substrate to enlarge the flakes. Although there was glue residue from the tape left all over the samples, the residue neither obstructed the Raman process nor damaged the film quality. Nevertheless, this type of graphene productions relies heavily on the choice of the substrate as it depends on the adhesive force and the contrast during mapping between graphene and the substrate. Normally, Si/SiO_2 is chosen as the substrate owing to the maximized contrast at human's optimal sensitivity.[18]

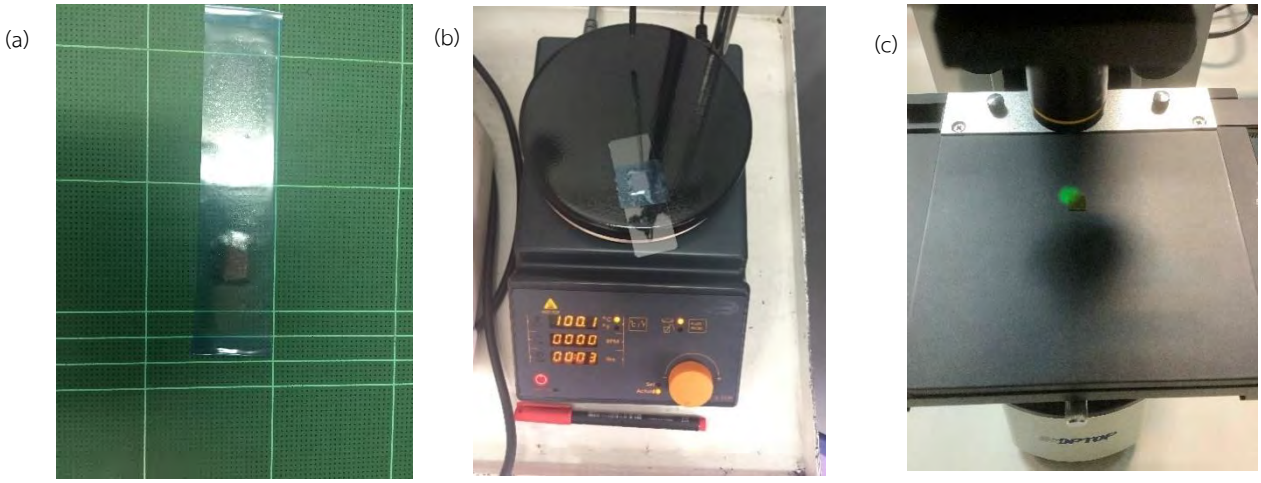

Fig 26. Graphite exfoliation process. (a) After a few times of sticking and peeling, FLG was deposited on VO_2/Al_2O_3. (b) The sample was heated at 100 °C for 2 minutes. (c) Searching for desirable flakes with a green-light mode to enhance contrast.

3.4 Raman spectroscopy

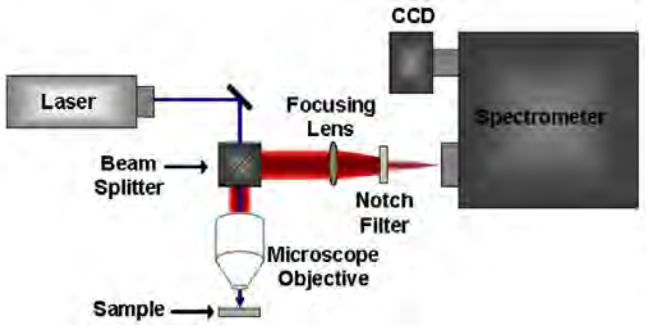

Fig 27. The schematic diagram of micro-Raman spectroscopy.[48]

Micro-Raman measurements were performed in backscattering configuration using a Horiba confocal modular Raman microscope with an iHR320 imaging spectrometer. A laser wavelength of 532 nm with no particular polarization was employed during the experiments. As shown in Fig 27., the light beam was focused on the sample via the microscope lens, and the scattered light went into the spectrometer. The notch filter would help pass the Strokes Raman scattering while the Rayleigh and anti-Stokes Raman scatterings were blocked. A diffraction grating inside the spectrometer then sorted out the scattered light according to the wavelengths, and finally a charge coupled device (CCD) detected the light and passed the signals to a computer for decoding.

3.5 Temperature-dependent Raman spectroscopy

Fig 28. Temperature-dependent Raman setup.

The temperature-dependent Raman characterization was carried out using a thermoelectric couple (called a mini-hotplate) which was heated by an electric current drawn from an adjustable-voltage power supply. The temperature was observed using a thermocouple which was firmly attached to the mini-hotplate. Both samples of bilayer-G/SiO_2 and bilayer-graphene/VO_2 were measured from 30 °C to 100 °C in 10 °C intervals (30-50 °C and 80-100 °C), and 5 °C intervals (50-80 °C). To minimize the difference between the surface temperature of the sample and the temperature measured from the mini-hotplate, the sample was kept away from disturbing air currents. Since the SPT was very sensitive, the intensity was kept lower than usual to ensure that the sample was not overheated. Unfortunately, the mini-hotplate was supplied with unstable current which, together with its resistance, resulted in temperature fluctuation, limiting the accuracy to $\pm$ 3.5 °C. Therefore, the T_{SPT} cannot be accurately calculated from this temperature-dependent experiment.

4. Results and discussion

4.1 VO_2/Al_2O_3 samples

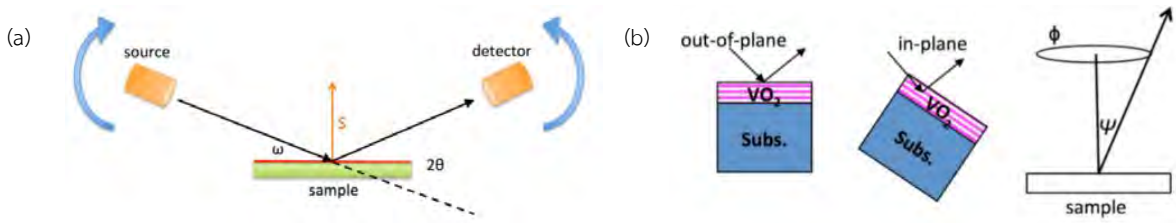

Fig 29. Schematic diagrams of (a) an out-of-plane XRD scan and (b) an in-plane XRD scan. For the out-of-plane XRD scan, the sample is placed parallel to the ground; meanwhile the source moves with respect to the sample at an angle ω and the detector moves simultaneously by an angle 2θ. For the in-plane XRD scan, the sample is tilted at an angle ψ for a desired lattice plane. The angle ϕ is scanned from 0° to 360°.[47]

From XRD measurements (characterized right after the deposition), both 50 and 100 nm VO_2 films deposited on c-Al_2O_3 exhibit single [010] orientation with respect to the underlying c-plane (0006) sapphire substrates (Fig 30.(a) and (b)). From the in-plane scans which can be used to determine the relative orientation of the film with respect to the substrate (Fig 30.(c) and (d)), there are 6 peaks of (011), and each of the orientations yields the corresponding 2 peaks. In other words, the VO_2/c-Al_2O_3 films are single-crystal like in the out-of-plane direction, but they are polycrystalline with 3 preferred orientations in the in-plane direction (parallel to the substrate surface). From the AFM results, the rms roughness values of the 50 and 100 nm VO_2 samples are 1.5 nm and 2.6 nm respectively. All in all, the obtained VO_2 samples show strong-textured crystallinity.[47]

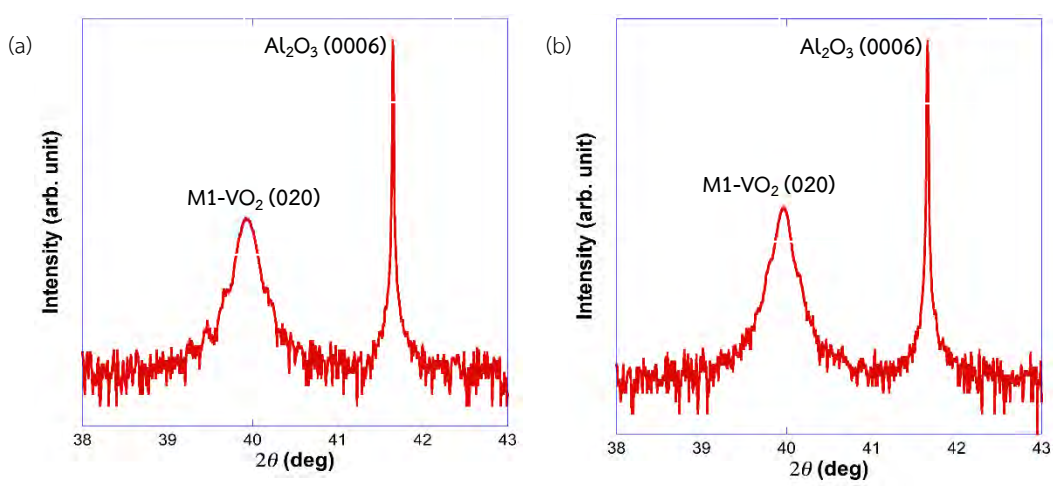

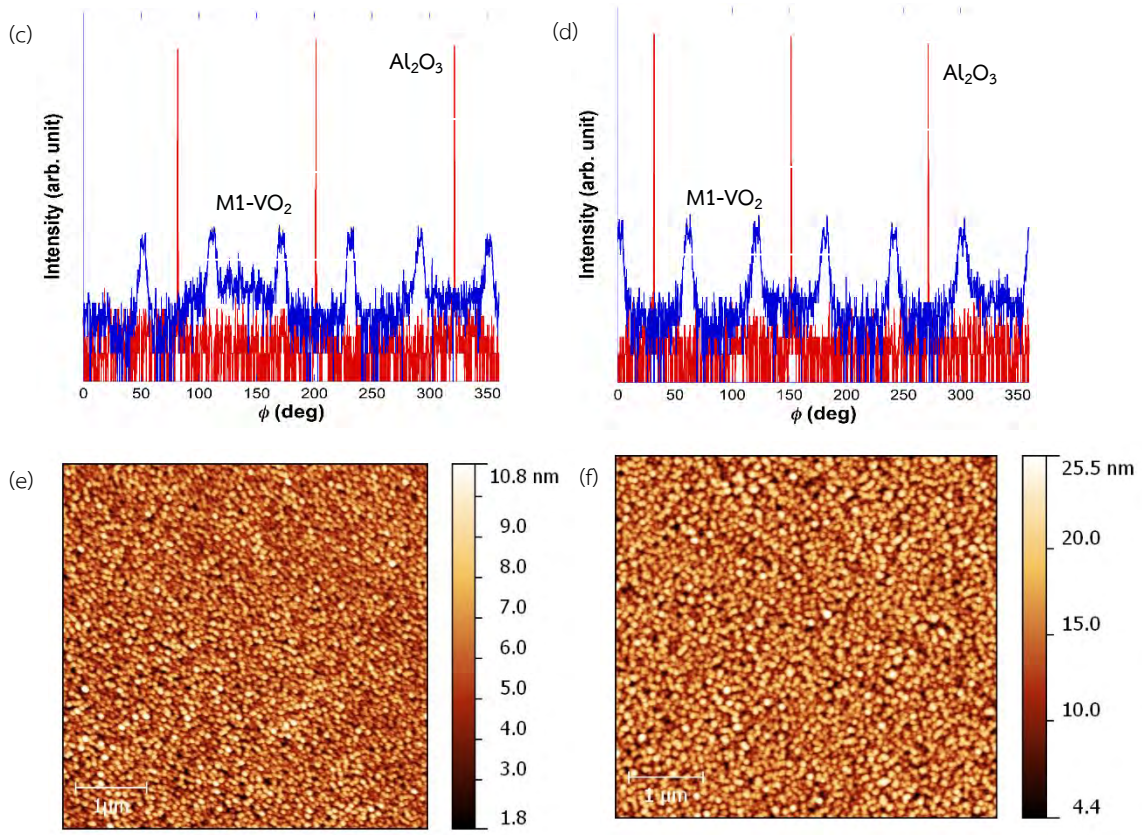

Fig 30. Out-of-plane XRD scans, in-plane XRD scans and AFM images of 50-nm (100-nm) VO_2 are a (b), c (d) and e (f) respectively. The rms roughness is 1.5 nm for 50-nm VO_2 and 2.6 nm for 100-nm VO_2.

4.2 Resistance vs temperature

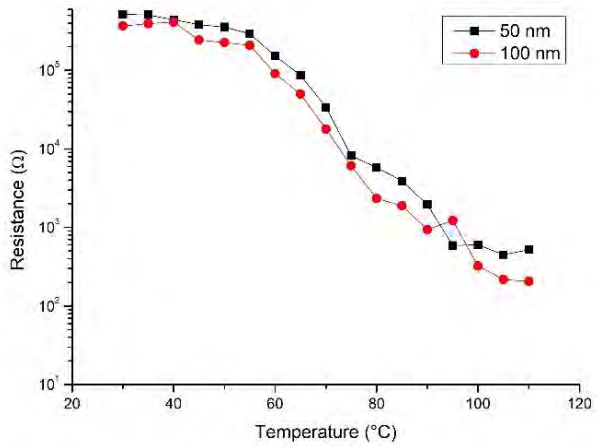

Fig 31. Resistance vs Temperature of 50-nm (black line) and 100-nm (red line) VO_2.

Across the MIT, the resistance drops by approximately 3 orders of magnitude as VO_2 changes from small-bandgap insulator to metal with an increase in carrier density.[2] (The resistance phase transition is a

hysteresis loop as in Fig 2.(b)). The raw data were differentiated directly to find the minimum value of $\frac{d[\log(\text{Resistance})]}{d(\text{Temperature})}$. Apparently, both 50 and 100 nm VO_2/Al_2O_3 have the average T_{MIT} value at 70±5 °C.

4.3 Raman spectra of VO_2/Al_2O_3

Before graphene deposition, Raman spectroscopy was performed with the 50-nm and 100-nm VO_2 samples. The obtained spectra in Fig 32. are in accordance with the reference spectra, confirming the existence of VO_2.[38] It can be seen that both 50-nm and 100-nm VO_2 samples exhibit similar Raman peaks. The fitted peaks of the most-pronounced Raman modes are also stated in Fig 32.

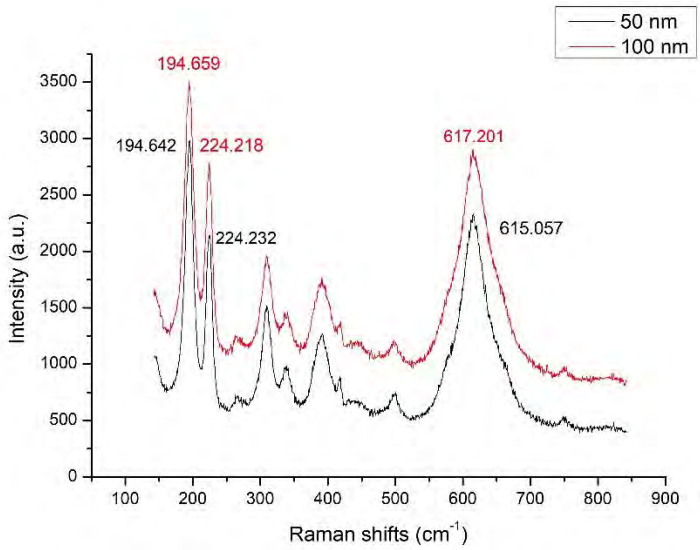

Fig 32. Raman spectra of 50 (black line) and 100 nm (red line) VO_2.

4.4 Graphite exfoliation

In spite of the green-mode light and various exfoliating approaches, low contrast between the flake and VO_2 made the flake-selection process very difficult and no monolayer graphene was found. However, there are some bilayer graphene available on both 50-nm and 100-nm VO_2 according to the Raman data. The successful bilayer flakes are depicted in Fig 33.

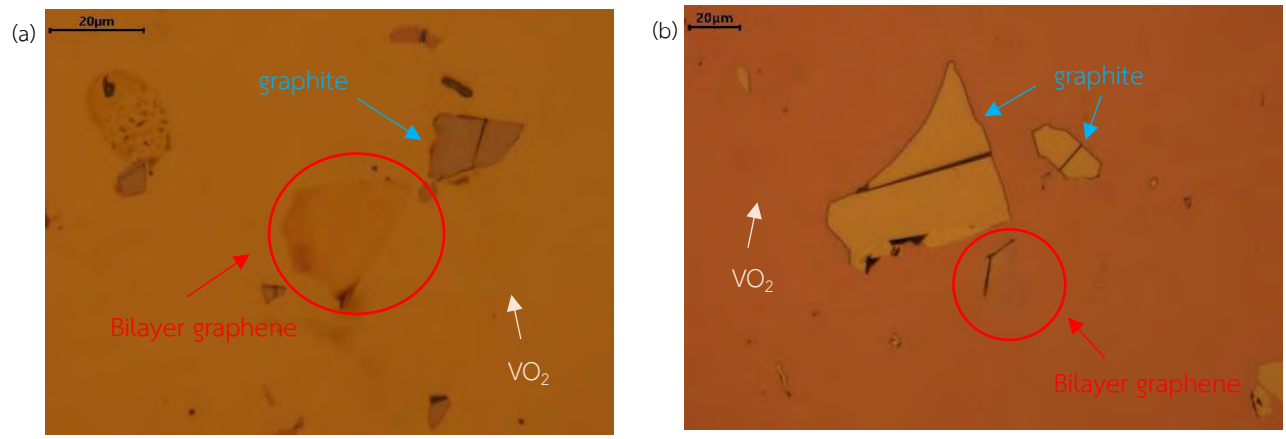

Fig 33. The bilayer-G/VO_2 (circled in red) hybrid structure with different VO_2 thicknesses of (a) 50 nm and (b) 100 nm.

4.5 Raman spectra of bilayer-graphene/VO_2/Al_2O_3

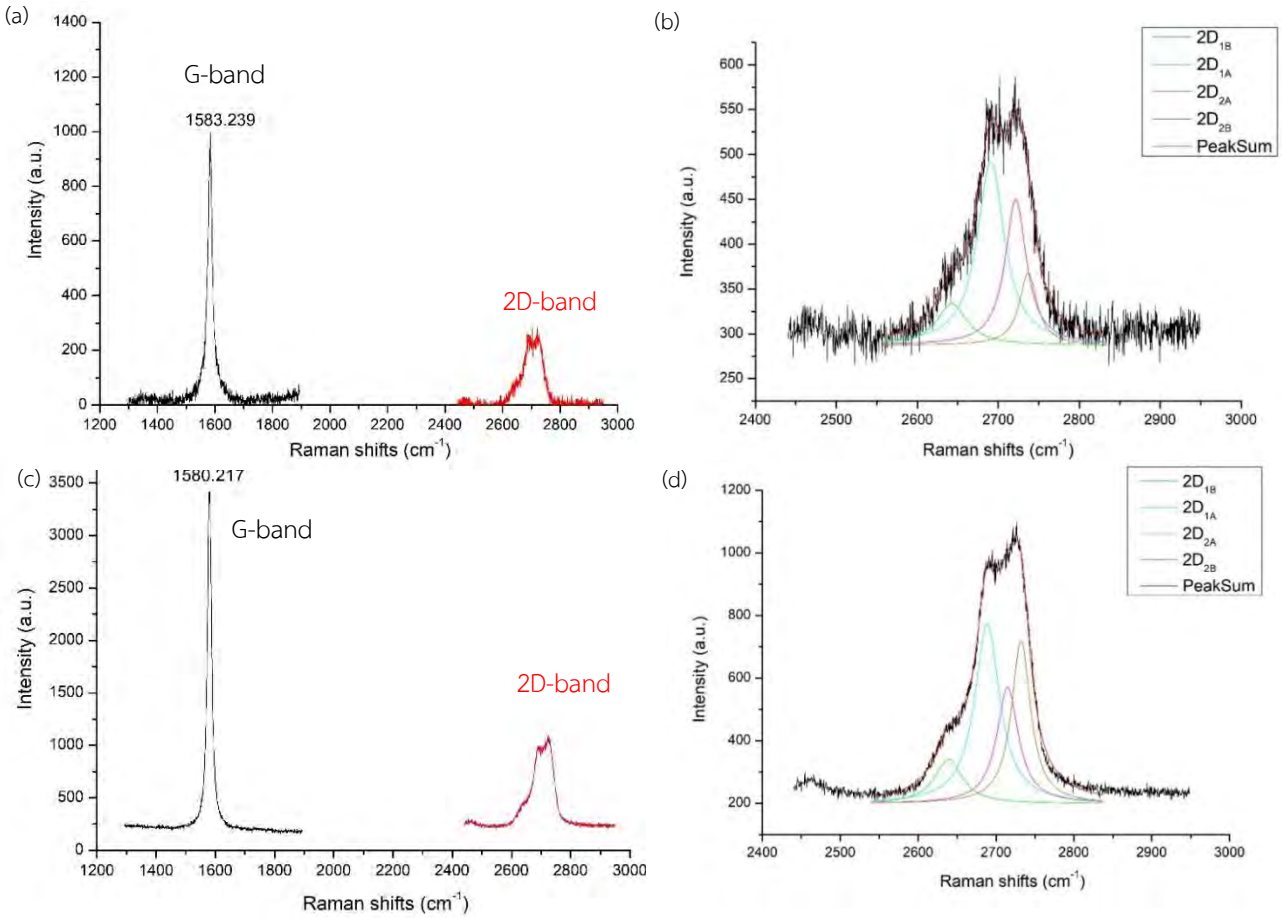

Fig 34. The Raman spectra of bilayer graphene are (a) and (b) for 50-nm VO_2, and (c) and (d) for 100-nm VO_2. In (a) and (c), both G-band (black line) and 2D-band (red line) are shown. In (b) and (d), the 2D peaks are fitted with 4 Lorentzian sub-peaks. The sub-peaks are colored differently in accordance to $2D_{1A}$, $2D_{1B}$, $2D_{2A}$ and $2D_{2B}$.

The G-band position of the bilayer-graphene/VO_2 is ~1583.24 cm^{-1} for 50-nm VO_2, whereas that of 100-nm VO_2 is lower at ~1580.22 cm^{-1}. If the lattice parameters of sapphire and graphene are considered, it is found that the lattice parameter of sapphire (0.479 nm) is smaller than that of graphene (0.492 nm), leading to the compressive strain in graphene. It is clear that graphene on the thinner VO_2, which has less strain relaxation compared with the thicker one, would be more subject to the compressive strain from the sapphire substrate, corresponding to the higher G peak position of bilayer-graphene/(50 nm)VO_2. The 2D-bands depicted in Fig 34.(b) and (d) could be fitted with 4 Lorentzian peaks, correctly contributing to the observed peak sums and demonstrating the Raman characteristic of bilayer graphene. Moreover, comparing these 2D-bands with the 2D-band of bilayer graphene of 2.33-eV (~532 nm) laser in Fig 24.(b), the resemblance is clear, indicating bilayer nature of graphene in the obtained bilayer-graphene/VO_2. However, it could be observed that the fitted $2D_{2A}$ intensity of the bilayer-G/(100 nm)VO_2 is lower than that of the $2D_{2B}$, contradictory to the explanation given in ref [43] which stated that the $2D_{(1,2)A}$ intensity is higher than that of $2D_{(1,2)B}$ due to the dominant q_A phonon scatterings.

Furthermore, shifting of the major Raman modes of VO_2 is shown in Table 1. All these modes experience blue shifts after the graphene deposition. For the low-energy modes at 194 and 224 cm^{-1}, there are slight shifts of approximately less than 1 cm^{-1} for both VO_2 thicknesses. In contrast, the high-energy mode at 612 cm^{-1} of 50-nm VO_2 blueshifts considerably about ~2.26 cm^{-1}. On the report of Nazari et al., shifting due to strain generally affects the 612 cm^{-1} vibration the most.[38] This was deduced from the Raman comparison among VO_2 on m, c and r sapphire substrates. As the sapphire substrates have different orientations, the amounts of strain induced in VO_2 are also different. From the experiment by Nazari et al., it turned out that the 612 cm^{-1} peak positions varied distinctly, while 194 and 224 cm^{-1} modes were approximately the same for all 3 orientations. Moreover, they also stated that the pronounced blueshift of 612 cm^{-1} mode at room temperature was attributable to the tensile stress parallel to the sapphire substrate plane, which produced compressive strain in the growth direction. Likewise, the blue shift in this case might derive from V-O bond shortening from the out-of-plane compressive strain in VO_2. Although the 612 cm^{-1} shifting of 100-nm VO2 exceeds others in the 100-nm spectrum, it is far less than that of the 50-nm one.

Mode	Peak Position (cm^{-1})	Type of Shifting		Δ (cm^{-1})	
		50 nm	100 nm	50 nm	100 nm
A_{1g}	~ 194	Blue shift	Blue shift	0.54	0.65
A_{1g}	~ 224	Blue shift	Blue shift	0.65	0.60
A_{1g}	~ 612	Blue shift	Blue shift	2.26	0.72

Table 1. Peak shifting after the graphene deposition. Δ represents the amount of peak shifting.

4.6 Temperature-dependent Raman spectra of bilayer-graphene/SiO_2, (100 nm)VO_2/Al_2O_3, and bilayer-graphene/(100 nm)VO_2/Al_2O_3

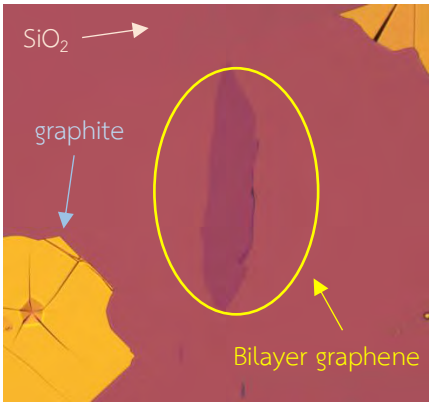

Fig 35. The bilayer-graphene flake on SiO_2.

Starting with bilayer-graphene/SiO_2, from the Raman data in Fig. 36(a) and(b), the red shift and decreasing FWHM with increasing temperature are spotted as expected from normal graphene on SiO_2 wafer.[29,49] These phenomena are associated with 2 interactions, namely the electron-phonon and the anharmonic phonon-phonon interactions. The electron-phonon scattering probability is proportional to the difference between the occupations of states below and above the Fermi level of graphene. Since the electron occupation transfers from the filled states to the empty states above the Fermi level with rising temperature, the scattering probability is lowered and hence the decreasing FWHM. It might also seem odd that the red shift of the G-band is present rather than the blue shift from a shorter bonding distance as usual, but the fact is that 4-phonon scattering dominates the system, leading to phonon softening.[50] Additionally, there is no significant change in the intensities for both G-band and 2D-band over the temperature range. The $2D_{1A}$ and $2D_{2A}$ peaks (the 2 highest peaks in the 2D-band) are more individually pronounced as the temperature increases (not peak splitting).

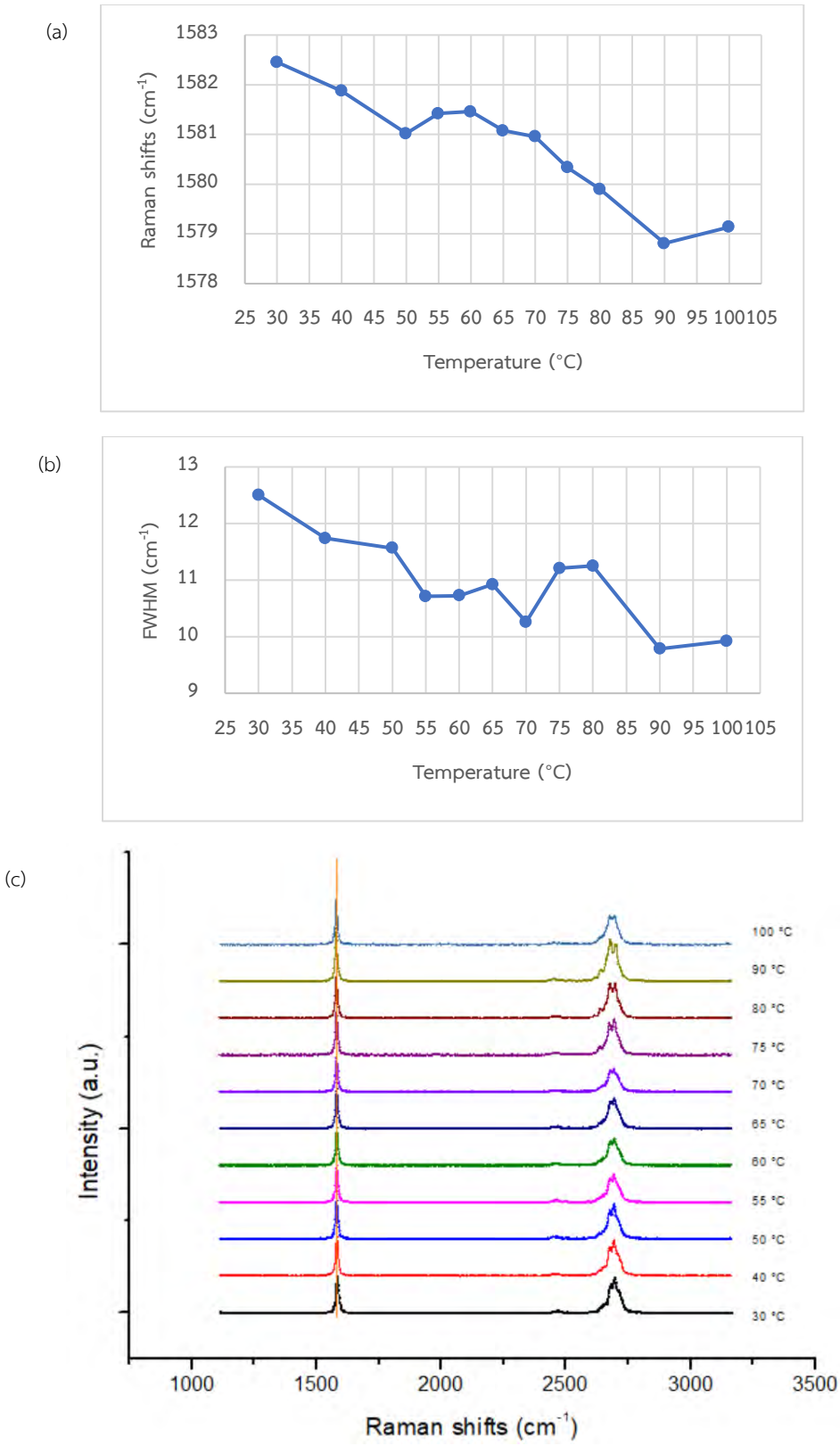

Fig 36. Temperature-dependent Raman spectra of bilayer-G/SiO_2. (a) G-band shifting. (b) FWHM as a function of temperature. (c) Raman shifts as a function of temperature. The temperatures shown are approximate with ±3.5 °C error.

For 100-nm VO_2 and bilayer-graphene/(100 nm)VO_2, the characteristic Raman shifts of VO_2 gradually fade with increasing temperature, become indiscernible with luminescence background above 55 °C, and completely disappear at 65 °C. It is clear that the intensities of the VO_2 spectra between 30-50 °C are more pronounced than those of bilayer-graphene/(100 nm)VO_2. On the other hand, above 50 °C to the transition point, the intensities and the peak shape of bilayer-graphene/(100 nm)VO_2 are more obvious than those of 100-nm VO_2. It cannot be seen whether graphene affects the T_{MIT} of VO_2 as both 100-nm VO_2 and bilayer-graphene/(100 nm)VO_2 undergo transition simultaneously in the temperature range 60-65 °C. Normally, the in-plane tensile strain would cause an increase in T_{MIT} of VO_2 as it leads to the increasing V-V distance along c_r axis and hence the destabilized metallic phase.[51] According to Zhou et al. and Kim et al., a decrease in T_{MIT} of VO_2 in the VO_2-graphene hybrid film is expected to result from electron injection and strain from different types of thermal expansion.[23-25] Therefore, it is likely that the fact that bilayer-graphene/(100 nm)VO_2, which is subject to the in-plane tensile strain, exhibiting no increasing T_{MIT} is due to a countereffect from electron injection from bilayer graphene. Furthermore, red shifts from all major modes of VO_2 with or without bilayer graphene are detected and shown separately in Fig 37.(a), (b), and (c). The red shifts of the low-energy phonon modes are anticipated according to ref. [38] which explained the effect of the mismatches in the thermal expansion coefficients. Moreover, the high-energy mode at ~620 cm^{-1} of bilayer-graphene/VO_2 blue shifts a little at first, then it plummets to around the red shift of its VO_2 counterpart at 55 °C. Recalling that the blue shift of the high-energy mode stems from the compressive stress from the M2 phase at the intermediate temperature, it is plausible that there is no partial transformation from M1 to M2 phase in this 100-nm VO_2 sample.

As for the G-band of bilayer graphene on 100-nm VO_2 (Fig 38.), the FWHM decreases with elevating temperature, in accordance with ref. [29], [49] and [50], and the bilayer-graphene/SiO_2 clarified earlier. Interestingly, the peak position shows the peculiar behavior, beginning with red shift and turning to blue shift at ~60 °C. This is unexpected, as the blue shift of the G-band normally originates from the in-plane compressive strain in graphene, but VO_2 itself has the positive expansion coefficient. Moreover, the intensities of the G-band and the 2D-band remain approximately the same through out the experiment.

It should be noted that the real sample temperatures would be slightly less than the reported values due to air gap interface.

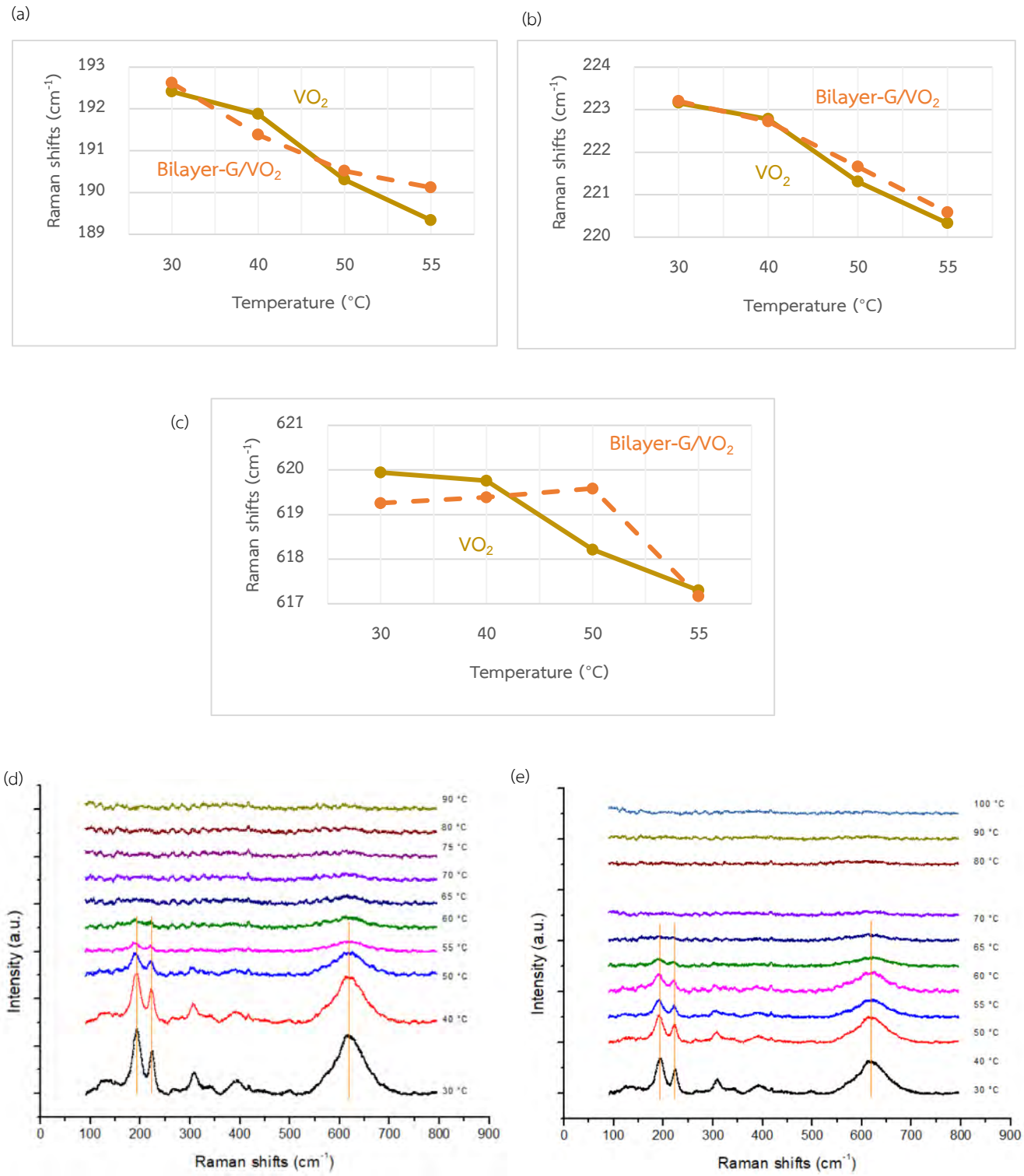

Fig 37. Raman shifts as a function of temperature of 100-nm VO_2 (solid line) and bilayer-graphene/(100 nm)VO_2 (dashed line) at (a) ~192 cm^{-1} mode, (b) ~223 cm^{-1} mode, and (c) ~620 cm^{-1} mode. Overall temp-dependent Raman spectra of (d) 100-nm VO_2 and (e) bilayer-graphene/(100 nm)VO_2. The temperatures shown are approximate with ±3.5 °C error.

(a)

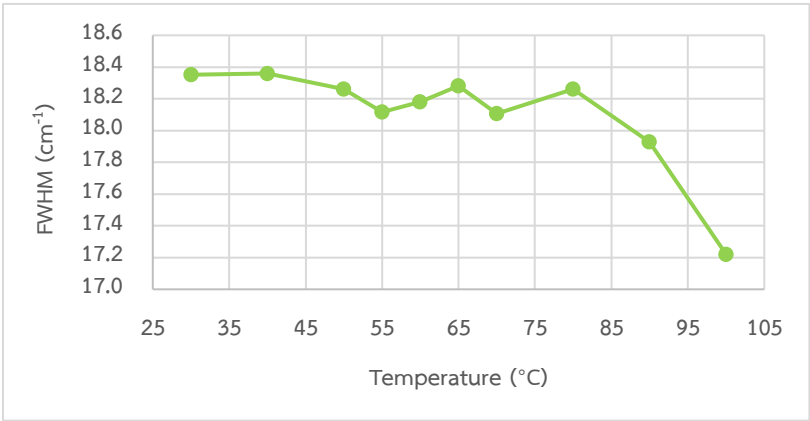

(b)

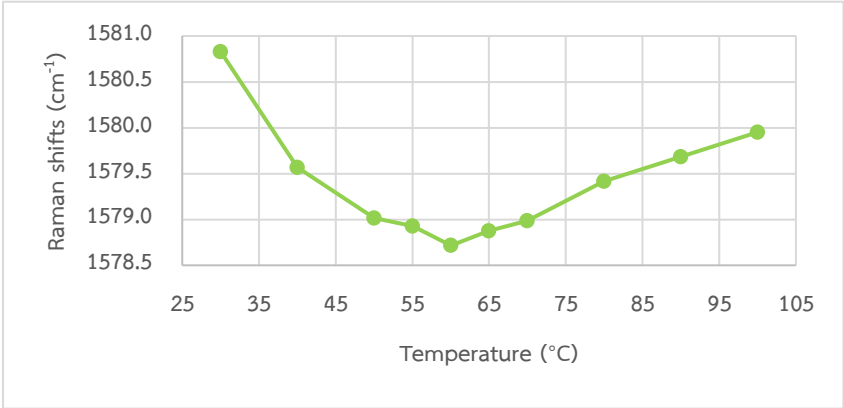

(c)

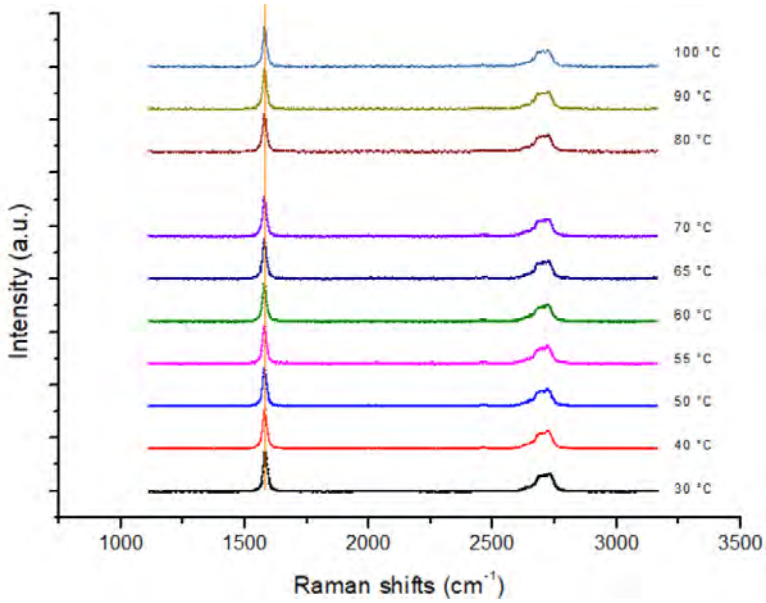

Fig 38. Temperature-dependent Raman of bilayer-graphene/(100 nm)VO_2. (a) FWHM of G-band as a function of temperature. (b) G-band shifts as a function of temperature. (c) Overall temperature-dependent Raman spectra of bilayer-graphene/(100 nm)VO_2. The temperatures shown are approximate with ±3.5 °C error.

5. Summary

It is evident that the hybrid structure of bilayer-graphene/VO_2 is excellent in terms of the crystal quality since VO_2 samples exhibit strong-textured crystallinity and there are no defect peaks found in Raman spectra of bilayer graphene on VO_2. There is no post-annealing at high temperature, hence graphene quality would not suffer from the oxidation. Moreover, VO_2 can be prepared by the RBTIBD method which allows highly-oriented crystallinity to avoid the effect of graphene wrinkles. However, the insufficient contrast between VO_2 and graphene makes it difficult to find few-layer graphene flakes, and almost impossible for the monolayer one. If the hybrid is to be developed for a large-scale production, other graphene depositions are required.

Depositing graphene on VO_2 clearly affects the strain in VO_2. The blue shifts of phonon energy from all 3 significant modes of VO_2 are observed, especially the largest upshift of V-O vibrations in the thinner (50 nm) sample. This might be attributable to the in-plane tensile stress or the out-of-plane compressive strain in VO_2. Simultaneously, the G-band of bilayer graphene on 50-nm VO_2 shows larger phonon energy than that on 100-nm VO_2, implying more compressive strain in bilayer graphene on 50-nm VO_2. Considering that the lattice parameter of the sapphire substrate is smaller than that of graphene and the thinner VO_2 sample is more vulnerable to the substrate clamping effect, it is reasonable to assume that the higher compressive strain in bilayer graphene on 50-nm VO_2 originates from the sapphire substrate. Furthermore, from the temperature-dependent Raman data, the SPT seems to occur before the MIT: the calculated T_{MIT} is about 70±5 °C, while the characteristic peaks of 100-nm M1-VO_2 vanish in the temperature range 60-65 °C. It cannot be concluded as to whether the hybrid with graphene reduces the T_{MIT} since the Raman spectra of both structures disappear in the same period between 60 °C and 65 °C. It is possible that the effect of the in-plane tensile strain in VO_2 with bilayer graphene on the increase in the T_{MIT} is overshadowed by the electron injection from graphene, the process which potentially reduces the T_{MIT}. For the 2 low-energy modes of VO_2, almost similar red shifts take place for both structures. However, the trends in the high-energy mode diverge, with the slight blue shift at the beginning of bilayer graphene/(100 nm)VO_2 before the massive downshift to the vicinity of the red shift of VO_2. Normally, VO_2 with M2 intermediate state would exhibit the high-energy blue shift due to the internal stress, so the VO_2 sample used in this experiment might be deemed transforming directly from M1 to R phase. The intensities of the G-band and 2D-band of this hybrid bilayer graphene/(100 nm)VO_2 remain roughly the same over the heating period; however, the G-band experiences the large red shift during the first half and then blue shift beyond the VO_2 approximate transition point. The result is actually in contrast with the normal shifting trend of the G-band, as it tends to red shift with the increasing temperature.

During the course of this research, VO_2 samples were fabricated and characterized via XRD and AFM beforehand at the University of Virginia, USA. The author has carried out graphite exfoliation, Raman spectroscopy and temperature-dependent Raman spectroscopy. There are many interesting details noted from the obtained results: the effect of the choice of substrates on the hybrid layers, the effect of the VO_2 film thickness on graphene, the effect of graphene on VO_2 and vice versa as observed from the strain in the materials and the transition behavior, and the peculiar blueshift with increasing temperature of graphene on VO_2.

References

[1] Eyert, V. (2002). The metal-insulator transitions of VO_2: A band theoretical approach. Ann. Phys., 11: 650-704. doi:10.1002/1521-3889(200210)11:9<650::AID-ANDP650>3.0.CO;2-K

[2] Shao, Z. Cao, Z., Luo, H., and Jin, P. (2018). Recent progress in the phase-transition mechanism and modulation of vanadium dioxide materials. *NPG Asia Materials*, 10: 581-605. doi: 10.1038/s41427-018-0061-2

[3] Soltani, M., Bah, S. T., Karmouch, R. Gaidi, M., and Vallée, R. (2019). Phase transition in thermochromic VO_2 coatings grown by ac dual magnetron cathode sputtering. *J Mater Sci: Mater Electron,* 30, 20043–20049. doi: https://doi.org/10.1007/s10854-019-02374-x

[4] Cao, X. and Jin, P. (2018). Solar modulation utilizing VO_2-based thermochromic coatings for energy-saving applications. *Emerging Solar Energy Materials.* doi: 10.5772/intechopen.75584

[5] Lee, S. H., Kim, M. K., Lee, J. W., Yang, Z., Ramanathan, S., and Tiwari, S. (2011). Vanadium Dioxide (VO_2) is also a Ferroelectric: Properties from Memory Structures. *11th IEEE International Conference on Nanotechnology.* doi: 10.1109/NANO.2011.6144602

[6] Ll'inskiy, A. V., Pashkevich, M. E., and Shadrin, E. B. (2017). Stage-by-stage modeling of the mechanism of semiconductor–metal phase transition in vanadium dioxide. *St. Petersburg Polytechnical University Journal: Physics and Mathematics,* 3(3): 181-186. doi: https://doi.org/10.1016/j.spjpm.2017.09.002

[7] Kramida, A., Ralchenko, Yu., Reader, J., and NIST ASD Team. (2019). *NIST Atomic Spectra Database (ver. 5.7.1).* National Institute of Standards and Technology, Gaithersburg, MD. Retrieved March 13, 2020 from https://physics.nist.gov/asd

[8] Keppler, H. (2018). Crystal Field Theory. In W. M. White (Ed.), *Encyclopedia of Geochemistry*. Springer, Cham. doi: https://doi.org/10.1007/978-3-319-39312-4

[9] Zhou, Y., Ha, S., and Ramanathan, S. (2015). Computation and learning with metal–insulator transitions and emergent phases in correlated oxides. In T. K. Liu and K. Kuhn (Eds.), *CMOS and Beyond: Logic Switches for Terascale Integrated Circuits (pp. 209-235)*. Cambridge: Cambridge University Press. doi: 10.1017/CBO9781107337886.013

[10] Aetukuri, N. P., Gray, A., Drouard, M., Cossale, M. Gao, L., Reid, A. Kukreja, R., Ohldag, H. Jenkins, C., Arenholz, E., Roche, K., Durr, H., Samant, M., and Parkin, S. (2013). Control of the metal–insulator

transition in vanadium dioxide by modifying orbital occupancy. *Nature Physics*, 9: 661-666. doi: 10.1038/nphys2733

[12] Kagoshima, S. (1981). Peierls Phase Transition. *Jpn. J. Appl. Phys*, 20(9): 1617-1634. doi: 10.1143/JJAP.20.1617

[13] Ihn, T. (2010). *Semiconductor Nanostructures*. New York, US: Oxford University Press Inc.

[14] Allen, P. B., Schulz, W. W., and Wentzcovitch, R. M. (1994). VO_2: Peierls or Mott-Hubbard? A View from Band Theory. *Physical Review Letter*, 72(21): 3389. doi: https://doi.org/10.1103/PhysRevLett.72.3389

[15] Laverock, J., Kittiwatanakul, S., Zakharov, A. A., Niu, Y. R., Chen, B., Wolf, S. A., Smith, K. E. (2014). Direct Observation of Decoupled Structural and Electronic Transitions and an Ambient Pressure Monoclinic like Metallic Phase of VO_2. *Physical Review Letters,* 113(21). doi:10.1103/physrevlett.113.216402

[16] Nelatury, S. (2018). *Graphene*. Retrieved March 20, 2020, from https://www.researchgate.net/figure/The-structure-of-graphene_fig1_323858855

[17] Yang, G. Li, L., Lee, W. B., and Ng, M. C. (2018). Structure of graphene and its disorders: a review. *Science and Technology of Advanced Materials*, 19(1): 613-648. doi: 10.1080/14686996.2018.1494493

[18] Soldano, C., Mahmood, A., and Dujardin, E. (2010) Production, properties and potential of graphene. *Carbon*, 48(8): 2127-2150. doi: https://doi.org/10.1016/j.carbon.2010.01.058

[19] Wang, J. Xu, X., Mu, X., Ma, F., and Sun, M. (2017). Magnetics and spintronics on two-dimensional composite materials of graphene/hexagonal boron nitride. *Materials Today Physics.* doi: https://doi.org/10.1016/j.mtphys.2017.10.003

[20] Rozhkova, A. V., Sboychakova, A. O., Rakhmanova, A. L., and Noria, F. (2016). Electronic properties of graphene-based bilayer systems. *Physics Reports*, 648: 1-104. doi: 10.1016/j.physrep.2016.07.003

[21] Ferralis, N. (2010). Probing Mechanical Properties of Graphene with Raman Spectroscopy. *Journal of Materials Science*, 45: 5135–5149. doi: 10.1007/s10853-010-4673-3

[22] McCann, E. Abergel, D.S.L., and Fal'ko, V. I. (2007). The low energy electronic band structure of bilayer graphene. *Eur. Phys. J. Spec. Top.*, 148: 91–103. doi: https://doi.org/10.1140/epjst/e2007-00229-1

[23] Kim, H., Kim, Y., Kim, T., Jang, A-R., Jeong, H.Y., Han, S.H., Yoon, D.H., Shin, H.S., Bae, D.J., Kim, K.S., and Yang, W.S. (2013). Electron transfer induced thermochromism in a VO_2–graphene–Ge heterostructure. *Nanoscale, 5*(7), 2632-2636. doi: 10.1039/c3nr34054f

[24] Kim, H., Kim, Y., Kim, T., Jang, A-R., Jeong, H.Y., Han, S.H., Yoon, D.H., Shin, H.S., Bae, D.J., Kim, K.S., and Yang, W.S. (2013). Flexible Thermochromic Window Based on Hybridized VO_2/Graphene. *ACS Nano,* 7(7), 5769-5776. doi: 10.1021/nn400358x

[25] Zhou , H., Li, J., Xin, Y., Cao, X., Baoa, S., and Jin, P. (2015). Enhanced optical response of hybridized VO_2/graphene films. *J. Mater. Chem. C, 3*(19), 5089-5097. doi: 10.1039/C5TC00448A

[26] Smith, E. and Dent, G. (2005). *Modern Raman Spectroscopy – A Practical Approach*. UK: John Wiley & Sons Ltd.

[27] Phys 774: Raman scattering. (2007). Retrieved March 25, 2020, from https://web.njit.edu/~sirenko/Phys-774/Lecture11-2007.pdf

[28] Wong, T. K. S. (2018). *Semiconductor Strain Metrology: Principles and Applications*. Bentham Science Publishers.

[29] Saito, R. (2019). Resonance Raman Spectroscopy of Graphene and Carbon Nanotubes. In R. B. Weisman and J. Kono (Eds.), *Handbook of Carbon Nanomaterials (Volume 9-10)* (pp.113-142). World Scientific Publishing Company.

[30] Nazari, M. (2013). Vibrational and Optical Properties of Vanadium Dioxide (PhD dissertation). Texas Tech University. Retrieved April 16, 2020, from http://hdl.handle.net/2346/58613

[31] Harima, H. (2002). Properties of GaN and related compounds studied by means of Raman scattering. *J. Phys.: Condens. Matter,* 14(38): 967-993. Retrieved April 16, 2020, from http://iopscience.iop.org/0953-8984/14/38/201

[32] Hollas, J. M. (2004). *Modern Spectroscopy*. UK: John Wiley & Sons Ltd.

[33] Barrow, R. F., Long, D. A., Millen, D. J., and Wilkinson, G.R. (1975). Raman Spectra of Solids. In R. F. Barrow, D. A. Long, and D. J. Millen (Eds.), *Molecular Spectroscopy: Volume 3* (pp. 433-496). Cambridge, UK: RSC Publishing.

[34] Srivastava, R. and Chase, L. L. (1971). Raman Spectrum of Semiconducting and Metallic VO_2. *Physical Review Letters,* 27(11). doi: https://doi.org/10.1103/PhysRevLett.27.727

[35] Shvets, P., Dikaya, O., Maksimova, K., and Goikhman, A. (2019). A review of Raman spectroscopy of vanadium oxides. *Journal of Raman Spectroscopy*, 50(8). doi: https://doi.org/10.1002/jrs.5616

[36] Schilbe, P. (2002). Raman scattering in VO_2. *Physica B,* 316–317: 600–602. doi: https://doi.org/10.1016/S0921-4526(02)00584-7

[37] Huanga, Y., Zhanga, D., Liua, Yi., Jina, J., Yanga, Y., Chena, T., Guana, H. , Fana, Ping., and Lv, W. (2018). Phase transition analysis of thermochromic VO2 thin films by temperature dependent Raman scattering and ellipsometry. *Applied Surface Science,* 456: 545-551. doi: https://doi.org/10.1016/j.apsusc.2018.06.125

[38] Nazari, M., Zhao, Y., Kuryatkov, V. V., Fan, Z. Y., Bernussi, A. A., and Holtz, M. (2013). Temperature dependence of the optical properties of VO_2 deposited on sapphire with different orientations. *Physical Review B*, 87(3): 35142-35148. doi: https://doi.org/10.1103/PhysRevB.87.035142

[39] Haberer, D. (2012). Electronic Properties of Functionalized Graphene Studied With Photoemission Spectroscopy (PhD dissertation). Retrieved April 10, 2020, from https://www.researchgate.net/publication/233409650_Electronic_Properties_of_Functionalized_Graphene_Studied_With_Photoemission_Spectroscopy

[40] Jorio, A., Cançado, L., and Malard, L. (2017). Vibrations in Graphene. In P. Avouris, T. Heinz, and T. Low (Eds.), *2D Materials: Properties and Devices*. Cambridge, UK: Cambridge University Press. doi: 10.1017/9781316681619.006

[41] Kostić, R., Mirić, M., Radić, T., Radović, M., Gajić, R., and Popović, Z.V. (2009). Optical Characterization of raphene and Highly Oriented Pyrolytic Graphite. *Acta Physica Polonica A,* 116(4). doi: 10.12693/APhysPolA.116.718.

[42] Malard, L. M., Guimarães, M. H. D., Mafra, D. L., Mazzoni, M. S. C., and Jorio, A. (2009). Group-theory analysis of electrons and phonons in N-layer graphene systems. *Physical Review B*, 79(12): 125426-125433. doi: https://doi.org/10.1103/PhysRevB.79.125426

[43] Ferrari. A. C. (2007). Raman spectroscopy of graphene and graphite: Disorder, electron–phonon coupling, doping and nonadiabatic effects. *Solid State Communications,* 143: 47–57. doi: https://doi.org/10.1016/j.ssc.2007.03.052

[44] Parka, J.S., Reinab, A., Saitoa, R.,Kong, J.,Dresselhausd, G., and Dresselhaus, M. S. (2009). G' band Raman spectra of single, double and triple layer graphene. *Carbon,* 47: 1303-1310. doi: 10.1016/j.carbon.2009.01.009

[45] Nguyen, A., Lee, J., Yoon, D., and Cheong, H. (2015). Excitation Energy Dependent Raman Signatures of ABA- and ABC-stacked Few-layer Graphene. *Scientific Reports*, 4(4630). doi: 10.1038/srep04630

[46] West, K. G., Lu, J., Yu, J., Kirkwood, D., Chen, W., Pei, Y., Claassen, J., and Wolf, S. A. (2008). Growth and characterization of vanadium dioxide thin films prepared by reactive-biased target ion beam deposition. *Journal of Vacuum Science & Technology A: Vacuum, Surfaces, and Films,* 26(1), 133–139. doi: 10.1116/1.2819268

[47] Kittiwatanakul, S. (2014). Study of Metal-Insulator Transition in Strongly Correlated Vanadium Dioxide Thin Films (PhD dissertation). University of Virginia, USA.

[48] Raja, P. M. V. and Barron, A. R. Raman and surface-enhanced Raman spectroscopy. Retrieved April 16, 2020, from https://chem.libretexts.org/Bookshelves/Analytical_Chemistry/Book%3A_Physical_Methods_in_Chemistry_and_Nano_Science_(Barron)/04%3A_Chemical_Speciation/4.03%3A_Raman_Spectroscopy

[49] Calizoa, I., Ghosha, S. Bao, W., Miao, Feng., Lau, C. N., and Balandin, A. A. (2009). Raman nanometrology of graphene: Temperature and substrate effects. *Solid State Communications*, 149: 1132–1135. doi: 10.1016/j.ssc.2009.01.036

[50] Bonini, N., Lazzeri, M., Marzari, N., and Mauri, F. (2007). Phonon Anharmonicities in Graphite and Graphene. *Physical Review Letters*, 99. doi: 10.1103/PhysRevLett.99.176802

[51] Muraoka, Y. and Hiroi, Z. (2002). Metal–insulator transition of thin films grown on (001) and (110) substrates. *Appl. Phys. Lett*. 80, 583. doi: https://doi.org/10.1063/1.1446215